Permission Sheet

I give permission for public access to my thesis for any copying to be done at the discretion of the archives librarian and/or the college librarian.

Signature:...................Moureen Kemei......................Date:......05/18/2010.........

Abstract

Fabrication and Characterization of Ferromagnetic Nanorings

Ferromagnetic nanorings are model systems for the study of magnetic phenomena in thin film structures. Unique closed flux states with potential applications in memory storage have also been observed in nanorings. A comprehensive understanding of the stability and the switching mechanisms of these novel states is important for data storage applications. We fabricate nanorings through electron beam lithography (EBL) to study the in-plane evolution of magnetic states in ferromagnetic ring structures. A systematic field dependent study of the nanoring states is performed using magnetic force microscopy (MFM). Micromagnetic simulations are used to suggest approximate fabrication dimensions and to interpret MFM results. We also explore a new method to control the vortex chirality in nanorings using a current generated magnetic field. In this technique, a magnetic field created by an atomic force microscope (AFM) probe placed at the center of the ring is used to manipulate the vortex chirality. Initial steps to the implementation of this technique have been performed and preliminary results are presented.

Fabrication and Characterization of Ferromagnetic Nanorings

Senior thesis presented to the faculty of Mount Holyoke College

Submitted by: **Moureen Kemei**

Advisors: **Prof. Kathy Aidala, Prof. Mark Peterson and Prof. Mark Tuominen**

Department of Physics - Mount Holyoke College

May 18, 2010

Acknowledgments

I would like to thank all the people who have contributed to the completion of this work. I thank my advisors, Kathy Aidala, Mark Peterson and Mark Tuominen for the opportunity to pursue research. I thank Prof. Kathy Aidala for introducing me to research and continuing to be my mentor and role model. Many thanks to Tianyu Yang who has taught me everything I know about fabrication and played an important role in obtaining results. I also thank Nihar Pradhan, for support and assistance during this thesis writing period. I thank my friend, Abby Goldman, who helped me to find the fun in research. I thank Abbey Litch for assistance with simulations and moral support. I thank members of Prof. Mark Tuominen's lab who welcomed me into their lab group. I also thank all the organizations that have funded this research including the Center for Hierarchical Manufacturing.

My sincere appreciation to Prof. Harriet Pollatsek, who has helped me navigate many challenges while pursuing the dual-degree engineering program. I thank Prof. Janice Hudgings and the Mount Holyoke Physics department for being so helpful through every situation. I thank my friends at Mount Holyoke who have added so much joy to my time here. I thank my host family for being my family over the last four years. I would like to thank all my family members whom I miss and love very much. Thank you for your love and support that motivates me everyday. I thank God for the strength to come this far and his continued love.

Contents

List of Figures

9

10

11

List of Tables

Chapter 1

Introduction and Motivation

We are constantly producing new data in the information age. Annually, the world generates more than an exabyte (10^{18}) of information[1] for storage. Additionally, complex systems with high data storage requirements such as computing architectures for complicated algorithms, digital archives for governmental institutions, Internet and photographic applications for mobile phones are constantly being developed. As a result, there is a pressing demand for high capacity data storage devices. Magnetic storage media store the highest percentage of data in comparison to other storage devices[1]. Research efforts are dedicated to discovering new methods to increase the capacities of magnetic storage devices at minimum costs.

Significant improvements in the design of high density magnetic storage media have been realized. Hard disk capacities of up to 1 terabyte as seen in the 7000 Deskstar^{TM} 7K1000 hard drive[2] from Hitachi have been achieved. Factors such as the miniaturization of magnetic bits, increase in bit density, design of sensitive read heads and a transition to perpendicular bit alignment have contributed to this increase. As bit densities increase and bit dimensions
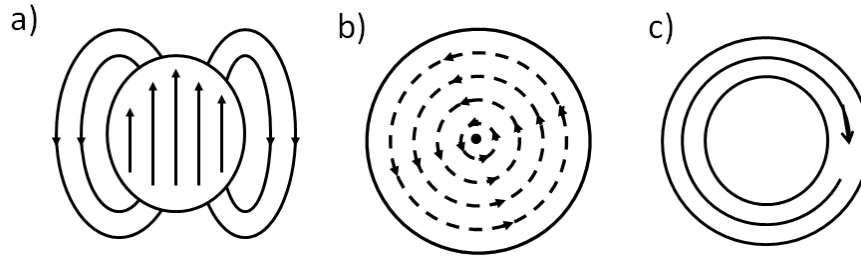
Figure 1.1: a) Ferromagnetic disk in the familiar dipole configuration. Stray field lines from the structure affect the region around the disk. b) The alignment of magnetic moments in the vortex state as observed in circular nanomagnetic disks. The structure has small stray fields at the center of the disk due to the high cost in exchange energy. c) The vortex state in a symmetric magnetic nanoring with no net stray magnetic field lines.

decrease, data distortion due to spontaneous magnetic state transitions in adjacent bits caused by stray fields and thermal effects are likely to occur. The spontaneous state transitions observed in extremely small ferromagnetic particles is known as superparamagnetism. The superparamagnetic limit marks the highest bit density where bit stability can be achieved. As we approach the superparamagnetic limit, patterned magnetic nanostructures have been proposed as future bit elements because they display closed flux states with minimum stray fields[3]. Closed flux states including the vortex state Figure 1.1 observed in ferromagnetic rings and disks with submicron dimensions minimize magnetic coupling between extremely close magnetic structures.

This thesis project is inspired by the fundamental physics of the novel magnetic states observed in ferromagnetic nanorings and their potential applications in magnetic storage media. We specifically explore the ring geometry because rings display the closed flux vortex state observed in nanodisks yet

lack the energetically costly vortex core present in disks. We systematically study the in-plane field dependent evolution of magnetic states in nanorings to determine the stable magnetization states of the rings as a function of their geometry. In addition, we are applying a new technique to control the magnetization of the nanorings using a current generated field.

Fabrication of nanorings with well defined shapes and no defects is challenging yet important in the study of magnetic states in nanorings. We fabricate ferromagnetic nanorings using electron beam lithography (EBL) at the University of Massachusetts, Amherst where the smallest nanorings have been fabricated[4]. Fabrication begins with spin coating a resist layer on a silicon substrate or a gold coated silicon substrate and patterning the resist layer using EBL performed in high vacuum by the JSM-7001F FESEM scanning electron microscope (SEM). Permalloy or Cobalt is then deposited by E−beam evaporation. To complete the fabrication process, lift-off is performed using acetone. The details of the fabrication process will be covered in Section 3.

We characterize the nanorings through magnetic force microscopy (MFM). MFM is a high resolution imaging technique that maps the magnetic force gradient between a magnetic scanning probe and a magnetic sample. MFM occurs in two steps. First, the probe determines the location of surface features by performing a height scan. Second, the tip is raised a certain height from the surface revealing tip deflections due to long-range magnetic forces between the tip and sample. A map of tip deflections versus probe position shows the magnetic configuration of the sample. MFM is sensitive to magnetic fields perpendicular to the sample surface. The variable field module (VFM) of the Asylum Research MFP3D atomic force microscope enables the study of the evolution of magnetic states in nanostructures in a changing in-plane field. Characterization is explained in detail in Section 4.4.

We are interested in a new approach where magnetic state transitions in ferromagnetic nanorings will be caused by a current generated field. This process involves applying a voltage on a conductive probe atomic force microscope (AFM) tip and placing the probe in contact with the conductive sample substrate at the center of a ring. To complete the circuit, the sample substrate is connected to ground through a resistor. The ground reference is common to both the AFM and the set-up resistor. An illustration of the set up is shown in Figure 1.2. The central field created by the conducting AFM probe is known as an Oersted field. Magnetic switching caused by an Oersted field has been simulated by Abby Goldman yielding approximate ring dimensions where magnetic state transitions occur at reasonable current densities. Simulations are performed using OOMMF (object oriented micromagnetic framework) provided by the National Institute of Standards and Technology [5]. Simulation results also assist in the interpretation of MFM images.

The study of patterned nanomagnets presents several challenges. Fabrication of structures with well defined shapes and dimensions of a few nanometers is difficult. Characterization of these structures requires high resolution magnetic force microscopy and is easily compromised by defects in the ferromagnetic nanostructures. Additionally, creating an Oersted field is a delicate task where the tip-sample connection is hard to achieve.
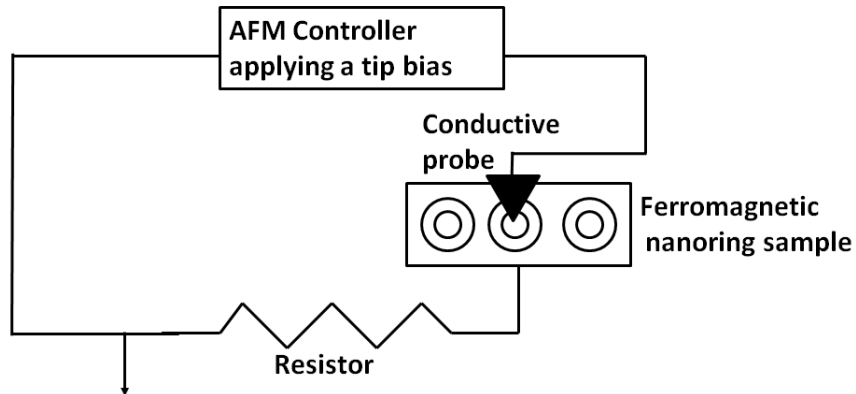
Figure 1.2: The implementation schematic showing the AFM tip placed at the center of the ferromagnetic ring.The ring sample is mounted on a conducting substrate and connected to a ground reference through a resistor to form a closed loop. The ground reference is common to both the AFM and the resistor.

1.1 Applications of ferromagnetic nanoring structures

1.1.1 The Hard Disk Drive

The first hard disk drive was designed by International Business Machines (IBM) in 1956 as a storage device for general purpose computers. The 305 RAMAC (Random Access Method of Accounting and Control) was the first hard drive; it could store 5 megabytes in 50 disks each with a radius of 24 inches. With time and progress in hard drive technology, hard drives have shrunk in size while boosting capacity, thus becoming more versatile, and are now used in cell phones and video games among others. A hard disk consists of several non-magnetic plates coated with a thin magnetic film. Digital in-

formation represented in binary numbers is stored in small magnetized units on the hard disk surface. The two common magnetic states, north and south, are used to represent binary digits. Each hard disk platter has a separate read-write head. Current flowing in the read-write head creates a local field that magnetizes the bit sections in the recording medium. When reading bits, the field sensitive read-write head senses the magnetization of the bits.
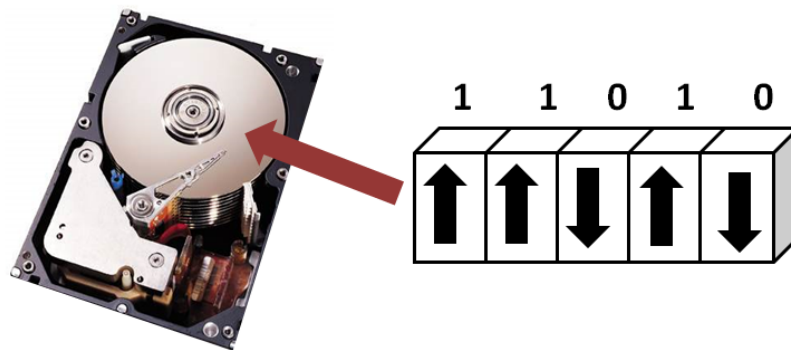
Figure 1.3: Internal configuration of the hard drive showing the read and write heads. Data recording in the two polarizations of a bar magnet is illustrated[6]

Advances in the hard drive industry have been achieved with the miniaturization of storage elements, improvements on read and write heads using new discoveries in magnetoresistance, a shift from parallel to perpendicular bit alignment and close packing of storage bits. Magnetic bit stability is compromised as bit sizes shrink and bit densities increase. Patterned nanomagnets such as nanorings are proposed as future bit elements because they demonstrate stable magnetic configurations with minimal stray fields.

1.1.2   Magnetic Random Access Memories (MRAM)

Random access memories (RAM) improve processing speeds by providing immediate data to microprocessors. The common forms of RAM employed in today's computers are static random access memories (SRAM) and dynamic random access memories (DRAM). Both DRAMS and SRAMs store information in integrated circuits that consume power and lose information when power is disrupted. The only non-volatile memory on a computer is the hard drive which has a much slower access time than the SRAM or the DRAM. Recently, there has been an attempt to replace DRAMs and SRAMs with the magnetic random access memory (MRAM) which is based on the magnetorestive effect. MRAMs are fast, have a high memory capacity, are non-volatile and consume less power in comparison to the SRAM and the DRAM[8].

MRAMs store data in magnetic states. One of the proposed designs for a memory unit in MRAM is the ring geometry, chosen because its circular shape eliminates sharp edge effects that may cause a large variation in bit switching fields. In addition, this geometry produces no stray fields in the vortex configuration where the magnetic moments curl around the circumference of the ring forming closed loops within the structure. The uniform switching fields postulated in nanorings are important for memory read and write operations. Additionally, unlike in disks where exchange energy increases quickly as the disks become smaller, the vortex state in magnetic nanorings can be maintained even for small outer ring radii because the exchange energy is slightly lower in nanorings compared to disks of the same outer diameter[9].

In this design, the MRAM is made of an array of multilayer structures consisting primarily of two magnetic layers separated by a thin insulating layer.
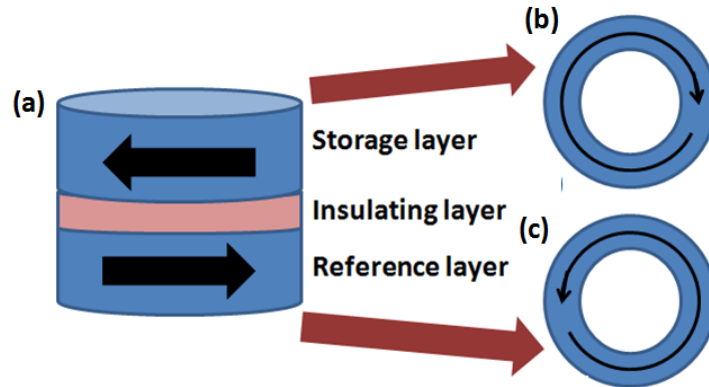
Figure 1.4: (a) Multilayer ring structure that would form the MRAM memory element (b) Clockwise vortex, magnetic state of the storage layer (c) Counter clockwise vortex that forms the magnetic state of the reference layer

The storage layer is a soft magnetic material layer whose configuration stores the binary digit while the reference layer maintains a preset state. Encoding information involves changing the magnetic state of the storage layer to reflect the polarization of the bit being stored. Magnetoresistance is used during reading by running current through the MRAM storage element and measuring the resistance. A higher resistance is expected when the magnetic moments in the reference and storage layer are aligned anti-parallel to one another.

A technique that will cause local magnetic switching in closely packed nanoscale MRAM elements without affecting nearest neighbors is still being studied. We explore magnetic switching in magnetic nanorings caused by the Oersted field from a conducting atomic force microscope (AFM) tip. This method could allow localized magnetic switching in nanorings at low current values improving the possibilities of MRAM applications in RAMs.

Chapter 2

Background and Theory

In this chapter, we explore the origin of magnetism in materials with a focus on ferromagnetic materials. We present a framework for understanding the range of magnetic states observed in circular thin film structures by analyzing the important magnetic energy terms which influence attainable states in nanorings.

Magnetism is fully explained by quantum mechanics. A simplifying model postulates that magnetic materials are made up of elementary point like and permanent magnetic moments (μ) [10]. The magnetic moment derives from a "current" resulting from intrinsic electron spin and the orbital momentum of electrons. Following the right hand rule, the polarity of the magnetic moment is given by the direction of the thumb when we curl the fingers of the right hand in the direction of the current. The overall magnetization(M) of a material is a vector defined as the sum of the dipole moments per unit volume.

$$\mathbf{M} = \frac{\sum_i \mu_i}{V} \tag{2.1}$$

Materials are magnetically classified by the preferred alignment of magnetic moments and the response of the magnetic moments to an applied field.

Diamagnetic materials assume a weak and oppositely polarized magnetization to that of an applied field. Paramagnetic materials assume a weak magnetic polarization in the direction of an applied field. Net magnetization of a diamagnet and a paramagnet exist only in the presence of an external field. Ferromagnetic materials are magnetized in the direction of the applied field and they retain a remanent state when the field is removed.

Long range ordering in ferromagnetic materials occurs due to a quantum mechanical effect known as exchange interaction, which causes adjacent electron spins to align parallel to one another for a given distance in a material. Regions of uniform magnetization in ferromagnetic structures are known as domains. Adjacent domains are separated from one another by domain walls. Before the application of a magnetizing field, the domains in a ferromagnet are usually arranged in different directions resulting in no net magnetization of the overall structure. In the presence of an applied field, the size of the domains polarized in the direction of the field increases. Magnetic saturation is attained when all the magnetic moments in a structure are oriented in the direction of the applied field.

Examples of ferromagnetic materials include Permalloy, Cobalt, Iron and Nickel. The magnetic behavior of a ferromagnet in a varying field is well described by a hysteresis loop. We could go around the loop beginning from a high positive field where we have magnetic saturation in the positive field direction indicated as M_s in Figure 2.1. We then decrease the field to 0 and the ferromagnet retains some magnetization in the previous field direction (M_r). Upon applying a negative field we reach 0 magnetization at the field H_c known as the coercive field. At high negative fields, we reach magnetization saturation in the negative field direction. When the negative field is removed the structure retains a remanent magnetization in the negative direction. At

the positive field H_c, the structure has 0 magnetization. High positive fields restore magnetic saturation in the positive direction, completing the hysteresis loop.

Ferromagnetic materials are thus well suited for memory applications because their present states reflect previous magnetizing fields. To restore the zero magnetization state in a polarized magnet, an opposite field of strength (H_c) must be applied. Hard and soft magnetic materials are distinguished by their coercivity. Hard magnetic materials have a high coercivity, thus they have much wider hysteresis loops and they make excellent permanent magnets. We are studying soft magnetic materials that have much narrower hysteresis loops characterized by low coercive fields, which are easy to achieve.
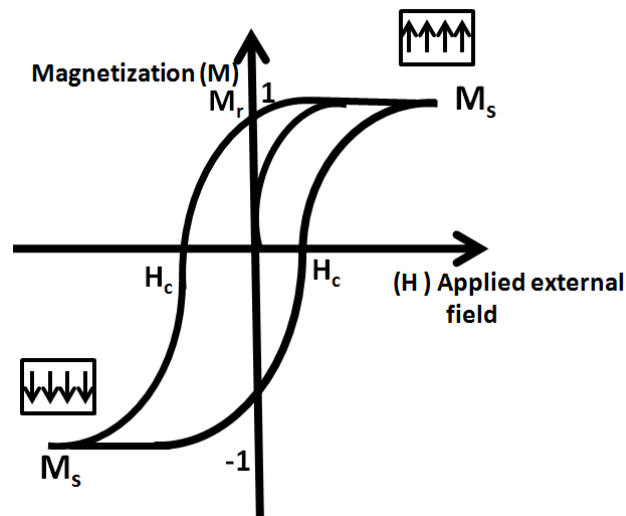
Figure 2.1: Hysteresis loop: The magnetization of a ferromagnetic material plotted against the applied field

2.1 Magnetic Energy

The magnetic states of submicron magnetic structures depend on the minimization of the main magnetic energy terms including: exchange energy, magnetostatic energy, crystalline anisotropic energy and the zeeman energy. The significance of the different energy terms depends on the size, shape and material of a magnetic structure[3].

2.1.1 Exchange Energy

Exchange energy ($U_{exchange}$) favors the parallel alignment of adjacent magnetic moments. This interaction is expressed in the Heisenberg interaction shown in Equation 2.2.

$$U_{exchange} = - \sum_{ij} J_{ij} \mathbf{S}_i \cdot \mathbf{S}_j \tag{2.2}$$

The exchange constant, J_{ij}, shows the strength of the interaction for two spins ($\mathbf{S}$) at positions i and j. The exchange constant is a positive value for ferromagnetic materials (Equation 2.2). Consequently, the lowest exchange energy is achieved when nearby spins are aligned parallel to each other. The minimum length in ferromagnetic materials where magnetic moments must align parallel to each other due to the exchange interaction is known as the exchange length.

2.1.2 Magnetostatic Energy

At the edge of a magnetized ferromagnetic material, field lines extend beyond the material forming closed loops. In fulfillment of Maxwell's Equation 2.3, magnetized materials have a demagnetizing field (H) whose value is the op-
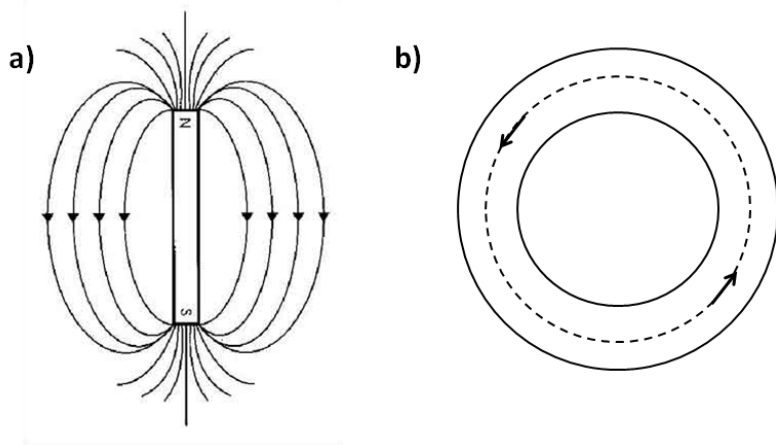
Figure 2.2: (a) A magnet in the familiar dipole configuration showing the diverging stray fields at the North and South poles of the magnet. This structure yields a high magnetostatic energy. (b) A schematic of the counter clockwise vortex chirality in a nanoring. This configuration does not have any magnetostatic energy. [12]

posite of the divergence of the magnetization of a structure[19] as shown by Equation 2.4.

$$\nabla \cdot B = 0 \tag{2.3}$$

$$\nabla \cdot H = - \nabla \cdot \mathbf{M} \tag{2.4}$$

Magnetostatic energy ($U_{magnetostatic}$) is related to the demagnetizing fields outside a magnetic element. The expression for magnetostatic energy is shown in Equation 2.5 where $\mu_\circ$ is the permeability of free space, M is the magnetization of the structure and H_d is the demagnetizing field.

$$U_{magnetostatic} = - \mu_\circ \int_{allspace} \vec{M} \cdot \frac{\vec{H}_d}{2} dV \tag{2.5}$$

Magnetostatic energy is minimized in closed flux states where magnetic field lines form closed loops within the structure thus nullifying the divergence of

the magnetization throughout the structure as illustrated in Figure 2.2.

2.1.3 Crystalline Anisotropic Energy

There is a preferred direction for the alignment of magnetic moments in a crystal lattice known as the easy axis. It is easier to magnetize a structure along the easy axis than along any other direction. It costs energy for magnetic moments to align in any other direction other than the easy axis. This is the crystalline anisotropic energy. This energy is significant in hard ferromagnetic materials such as magnetite and high-carbon steel while it plays a less significant role in soft ferromagnetic materials such as iron, cobalt and iron [3]. Figure 2.3 shows the preferred direction of magnetization in the crystal lattice of iron, nickel and cobalt. The cobalt crystal is almost at its saturation magnetization along the 100 crystal direction at extremely low fields while it requires much higher field to attain saturation along the 001 crystal direction. Of the three metals, crystalline anisotropy plays the greatest role in the magnetization of cobalt.
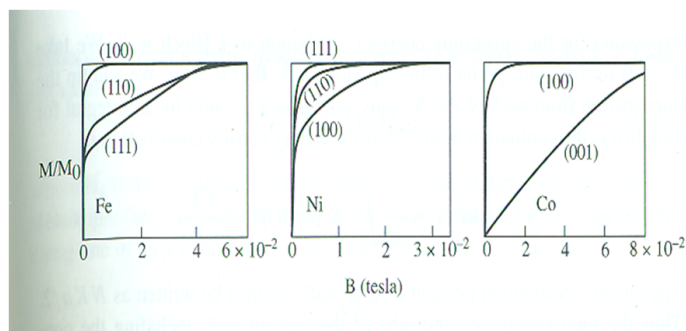
Figure 2.3: Magnetization in Iron, Cobalt and Nickel for applied fields in different directions demonstrating anisotropy. [19] S. Blundell p. 131

26

2.1.4 Zeeman Energy

In the presence of an applied field, a new energy term known as the Zeeman energy (U_{Zeeman}) becomes important. The Zeeman energy is very similar to the magnetostatic energy (Equation 2.5) except that instead of the demagnetizing field (H_d), the expression now involves the applied field (H_a). The Zeeman energy is given by Equation 2.6 where $\mu_\circ$ is the permeability of free space, M is the magnetization of the structure and H_a is the applied field.

$$U_{Zeeman} = - \mu_\circ \int_{allspace} \overrightarrow{M} \cdot \frac{\overrightarrow{H_a}}{2} dV \tag{2.6}$$

As illustrated in Equation 2.6, this energy is minimized when the magnetic moments of a magnet are aligned in the direction of the applied field.

2.2 Magnetic Configurations in Nanorings

Magnetization in nanorings favors the configuration with the lowest energy. The total energy is the sum of all the magnetic energy terms as shown by Equation 2.7. The importance of the different energy terms can be controlled by changing the shape, size and material of a structure.

$$U_{tot} = U_{exchange} + U_{magnetostatic} + U_{anisotropic} + U_{Zeeman} \tag{2.7}$$

We are studying the magnetic configurations of rings made of Permalloy. Crystalline anisotropic energy is often negligible in soft magnetic materials. The nanorings are polycrystalline. In polycrystalline geometries, the anisotropic effect of individual crystals is zeroed out in the overall structure[11]. There is a careful balance between the exchange and magnetostatic energy where slight changes lead to a variety of in-plane configurations in nanorings.

2.2.1   Single Domain State

The single domain state represents uniform magnetization in the ring. Two configurations, the dipole and vortex state, are single domain states observed in magnetic nanorings.

The dipole state is the preferred configuration in structures with dimensions of a material's exchange length and in structures exposed to high external fields. At high external fields, the Zeeman energy prevails, aligning all the magnetic moments in the direction of the field. Dipole states minimize exchange energy because adjacent spins are parallel to one another. However, magnetostatic energy increases as the stray fields of a structure increase.

In the vortex state, the magnetic moments curl around the circumference of the ring, forming closed loops. This is a stray field—free stable state that occurs in two forms based on the vortex chirality, which could be either clockwise or counterclockwise. This state represents the lowest overall energy of a ring. Exchange energy is minimized because adjacent spins are almost parallel and no magnetostatic energy is realized because there are no stray fields. This state is favored in wider rings where the stray field from the structure in the dipole state is energetically unfavorable. In contrast, the dipole state may remain stable in narrower rings because the exchange interaction is more important than the magnetostatic effect of the stray fields from the structures.

The vortex state has been proposed as a potential data storage state with the chirality representing the two bit states for the following reasons. This stray field—free state is immune to the superparamagnetic limit. A 10nm diameter ring array with a 10nm spacing between rings, can reach densities as high as 0.25Tbits/cm^2 [13]. The vortex state is stable in rings with a diameter
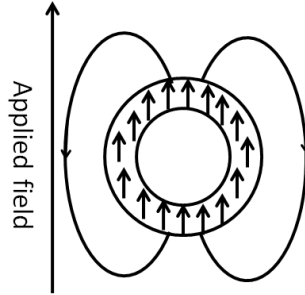
Figure 2.4: Alignment of magnetic moments in a ring structure in the dipole configuration in an external field
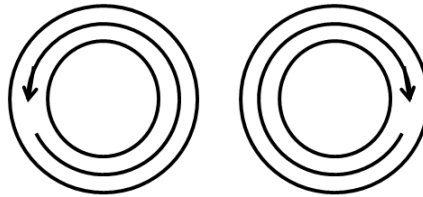
Figure 2.5: Vortex state in rings. The clockwise and counterclockwise vortex states are shown

as small as 10nm, while it is only stable in magnetic disks with a diameter greater or equal to 100nm because in smaller disks there is a high cost in exchange energy due to the presence of the vortex core. A vortex core is the central region on a disk in the vortex state where the magnetic moments pop out of the plane of the disk to reduce exchange energy. Simpler and repeatable switching mechanisms are expected in ring geometries in contrast to disks because of they do not have a vortex core.

2.2.2   Multiple Domain Configurations

Single domain states are stable in elements with dimensions in the range of a material's exchange length. However, as the dimension of an element in-

29
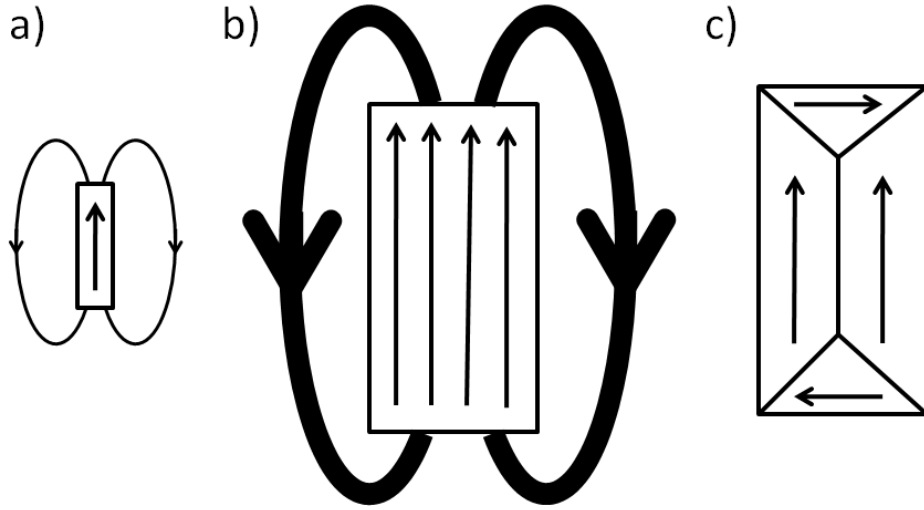
Figure 2.6: (a) Uniform magnetization in a structure with the dimensions of a single domain. (b) High magnetostatic energy is expected in multiple domain structures in the uniform magnetization state. (c) Formation of domain walls minimizes the magnetostatic energy by breaking the overall magnetization into smaller domains creating a closure domain structure.

creases there is an increase in the magnetostatic static energy. At a certain point, magnetostatic energy becomes so high that lower energy states can be formed by breaking the uniform magnetization of the structure creating several domains. Domains are smaller regions of uniform magnetization in a large magnetic structure. The transition regions between two domains is known as a domain wall. At the domain walls, there is a high cost in exchange energy due to the misalignment of magnetic moments. However, the multi−domain state at times gives a lower overall energy for a magnetic structure in comparison the uniform magnetization state which yields high magnetostatic energy as illustrated in Figure 2.6.

Since domain walls cost energy, smaller domain walls are preferred to

larger domain walls. In fact, domain wall energy minimization has been exploited to control chirality in asymmetric rings by applying an in-plane field in the direction of asymmetry. The domain walls prefer to annihilate in the narrowest ring width. In general, the type of domain walls formed in a structure depend on the geometry of the structure and defects that trap domain walls.

Onion State

In the presence of a strong magnetic field, ferromagnetic rings attain the dipole state. The onion state is the relaxation configuration when the saturating field is removed. This state is characterized by two domains with opposite chirality separated by a head to head domain wall and a tail to tail domain wall as illustrated in Figure 2.7. These domain walls are 180° apart. The domain walls observed in the onion state are categorized into
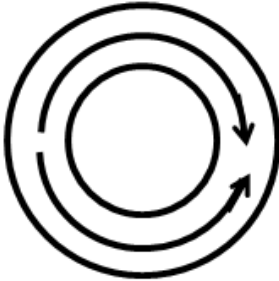
Figure 2.7: Arrangement of magnetic moments in the onion state. Two domain walls 180° apart are formed in this configuration.

two: vortex walls observed in wider rings and transverse walls expected in narrower rings [13]. Transverse domain walls are characteristic in narrower rings where high exchange energy prevents the formation of vortex domain
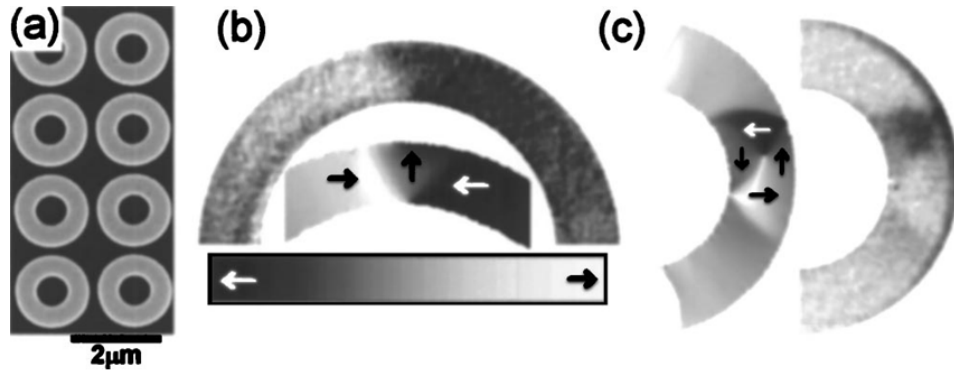
Figure 2.8: a) An array of polycrystalline Co rings imaged by scanning electron microscopy. The rings have an outer diameter=1.65 μm, width=530nm and thickness=34nm. b) High resolution photo emission electron microscopy (PEEM) images and micromagnetic simulations of Co rings with a width=260nm and height=10nm showing a transverse domain wall. c) PEEM and micromagnetic simulation images of rings with a width=350nm and height=34nm showing a vortex domain wall.[15]

walls. In wider rings, vortex walls are preferentially nucleated because of the high magnetostatic energy that would result if transverse domain walls were formed. Experimental and simulation data demonstrating this observation are indicated in Figure 2.8[15].

The above simulation and experimental results show transverse wall formation in a narrow ring and vortex wall formation in a wider ring. During photo emission electron microscopy (PEEM), the imaging technique used in the above experiment, circularly polarized X-rays are directed onto the sample. Secondary electrons from the sample reflect the spin orientation of the magnetic structure and are used to generate the magnetic contrast illustration of the domain walls. The simulations were performed using object oriented

micro magnetic framework (OOMMF)[5].

Twisted State

In addition to the onion, vortex and dipole states, several unstable states have also been observed in ring. The twisted state is a metastable state that has been experimentally imaged and simulated in narrow rings [14]. In this
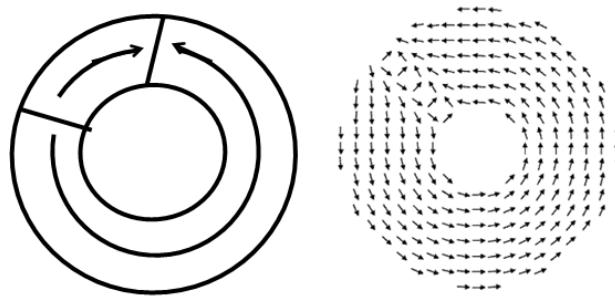
Figure 2.9: Magnetic moments in the twisted state. In this state, two domain walls appear adjacent to one another

configuration two interacting domain walls appear close to each other without annihilation due to a high cost in exchange energy. Single or multiple 360° domain walls are formed in the twisted state. The two domain walls are attracted to each other because they have opposite circulation yet they are unable to annihilate because the walls are separated by a constant distance maintained by the exchange energy between the two walls. A large field will overcome the energy barrier causing the walls to annihilate.

2.2.3   Switching Mechanisms

In a varying magnetic field, state transitions occur in ferromagnetic structures forming different magnetization configurations at each field value

as determined by the competition between exchange and magnetostatic energy. Ring hysteresis displays two main switching processes, namely the onion rotation process (O) and the vortex formation process (V). In the O process, the two domain walls of the onion state move opposite to each other. Magnetization reversal occurs by the 180° rotation of the domain walls as directed by the external field. In the O process, the domain walls remain 180° apart throughout the hysteresis. In the V process, the domain walls of the onion state move towards each other as the magnetizing field decreases. The domain walls annihilate forming the vortex state for smaller field values. At the opposite high field, the opposite onion state is formed. There is a large change in magnetization during the transition from the dipole state to the vortex state as well as from the vortex state to a dipole state.The V process is dominant in wider rings while the O process is prevails in narrow rings.

The bistability between the two reversal processes depends on the competition between exchange and magnetostatic energy. In narrow rings, exchange energy dominates prohibiting the annihilation of the two domain walls and the onion rotation process is preferred. In wider rings, high magnetostatic energy in the onion state is minimized when the two domain walls annihilate forming the vortex state. The two processes can occur with equal probability in symmetric rings; the occurrence of either process is determined by the ring parameters. In asymmetric rings, the reversal process can be controlled by the direction of the applied field. When the magnetic field is applied along the asymmetric axis, magnetic reversal by the V process is guaranteed. Asymmetry allows the manipulation of magnetic reversal process because domain wall energy depends on the ring width. The wider the ring region, the greater the domain wall energy. Therefore the domains move towards the narrowest ring width.

Micromagnetic simulations of the hysteresis curves resulting from the two magnetization reversal process have been performed by Zhu et al; the results of their work is presented in Figure 2.10. Figure 2.10. (a) is a simulation of the hysteresis of magnetization reversal through the V process while Figure 2.10 (b) shows the hysteresis of magnetization reversal through the O process. These simulations use the Landau-Lifshitz-Gilbert equation to evaluate the minimum energy configuration. In Figure 2.10 (c) controlled magnetic reversal in cobalt asymmetric rings is demonstrated. We observe that the hysteresis curve of the rings when the field is along the asymmetric axis is similar to the hysteresis of the V process while the hysteresis curve is closer to that of the O process when the field is applied along the symmetric axis. These measurements were performed by a 10 vector vibrating magnetometer at room temperature. In symmetric rings magnetic reversal is independent of θ. Controlling domain wall motion in asymmetric rings by changing the direction of the external field is one way to control chirality in asymmetric nanorings.
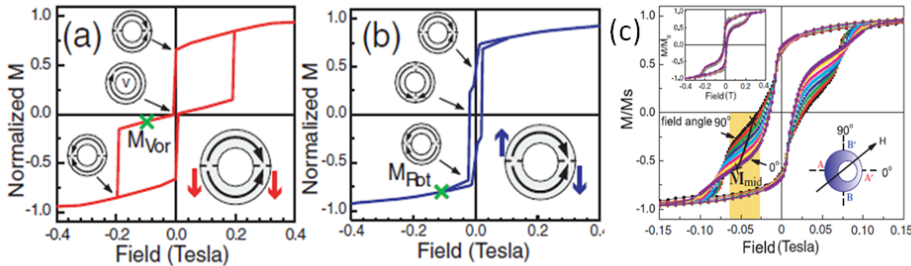
Figure 2.10: Hysteresis curves of the two magnetization reversal processes. (a) The vortex rotation process. (b) The onion process. (c) Magnetization reversal of asymmetric rings at different angles of the applied field. (inset)Independence of the magnetization reversal to the applied field angle in symmetric rings. [8]

2.3 Oersted Field

A direct way to control chirality in ring structures is through an Oersted field. An Oersted field is the circular field generated by a conducting wire. We would like to approximate the Oersted field from an infinite conducting wire placed at the center of the ring with the field generated by a conducting atomic force microscope probe placed at the center of the ring. The field decreases in strength as you move further from the center of the ring. An approximation of the field strength at a distance r for current I is given by Equation 2.8

$$B = \frac{\mu_\circ I}{2\pi r} \tag{2.8}$$

The experimental implementation of this technique involves using a solid metal atomic force microscope probe placed at the center of the ring to generate the magnetic field. This new technique can be used to control vortex chirality in symmetric and asymmetric rings alike. We will discuss in detail the implementation of this technique in Section 5.3

2.4 Micromagnetic Modeling

Micromagnetics describes magnetization at length scales bigger than that of atomic spins yet small enough to demonstrate magnetic interactions between individual magnetic moments. These interactions depend on magnetic energies namely: exchange, magnetostatic, crystalline anisotropy and Zeeman energy. The equation that describes the time evolution of the magnetization $\mathbf{M}$ of a finite element of magnetic material is the Landau Lifshitz equation shown in Equation 2.9. $\mathbf{H}$ is the total magnetic field that includes all the magnetic energy contributions, M_s is magnetic saturation, γ is the gyromagnetic ratio

36

and α is the dimensionless dissipation coefficient. This equation describes the time evolution of the magnetic moments into the preferred configuration.

$$\frac{d\mathbf{M}}{dt} = \gamma \mathbf{H} \times \mathbf{M} + \frac{\gamma\alpha}{\mathbf{M_s}}(\mathbf{M} \times \mathbf{H}) \times \mathbf{M} \tag{2.9}$$

Simulations of magnetization in nanomagnets are important because they predict approximate dimensions where certain states can be expected as well as the approximate fields at which transitions occur. Simulations also describe the dynamic transition between states, displaying intermediate states. While energy minimization reveals the preferred magnetic state, time evolution of magnetic states reveals that metastable states such as the twisted state occur in thin ring structures instead of the favored low energy vortex state. The twisted state occurs when two domain walls are moving towards each other; however, at a certain separation of the domain walls high exchange energy prevents the annihilation of the domain walls. The ring gets stuck in this metastable configuration. Simulations also help us interpret magnetic force microscopy images.

2.5   Previous Work

Ferromagnetic nanorings have received much attention in recent years because of their potential for memory applications as well as the promise for novel magnetic phenomena in thin film ring structures. Some of the unique properties of nanorings include uniform switching fields because rings do not have a vortex core or sharp edges that contribute to a wide distribution of switching fields. Rings also display stray field−free states such as the vortex state that are important to the design of high density storage media.The study of ferromagnetic nanorings has progressed with advancements in fabri-

cation techniques, development of high resolution magnetic characterization techniques such as magnetic force microscopy (MFM) and the design of reliable simulation methods that have assisted in interpretation of data as well as predicted novel states in these thin film structures. We look at some of the work done in nanorings that relates to our research objectives.
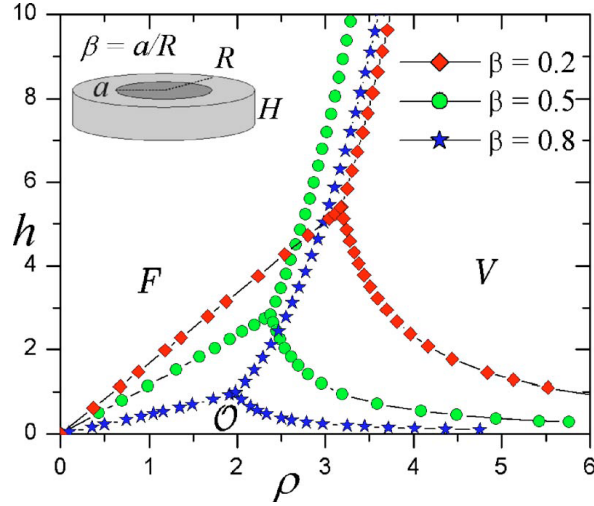
Figure 2.11: For rings of varying width, the stability of the onion state (O), vortex state (V) and out of the plane magnetization (F) is explored as a function of the outer diameter of the ring and the ring height [17]

We are examining how ring magnetization depends on geometry. Theoretical studies were performed by Landeros et al. [17], exploring the magnetic configurations of microrings as a function of the ring geometry. The stability of the three magnetic states: the vortex state, the onion state and magnetic saturation along the ring axis are studied as a function of the ring dimensions. These computations consider exchange and magnetostatic energy. Crystalline anisotropic energy is neglected because it has no overall effect in polycrystalline structures. The computations define the dimensions (R) as the external ra-

dius, the internal radius (a), the exchange length (L_{ex}) and the ring height (H). Dimension less quantities are preferred to eliminate material effects; quantities such as $\rho = R/L_{ex}$, $h = H/L_{ex}$ and $\beta = a/R$ are defined. β relates to the width of the ring, thin rings have high β values while thick rings have low β values. Results are presented in the phase diagram Figure 2.11. The total energy calculations for a given ring geometry in the three possible states are computed. The lowest energy configuration is determined and used in the phase diagram, which shows the state with the lowest energy configuration for a given ring geometry.

The results propose that the onion state is more stable in thin rings than it is in thicker rings. Figure 2.11 shows the onion state as stable in rings with a height less than ≈ 5 exchange lengths. The out-of-plane single domain state is preferred in rings with a smaller outer diameter (ρ) yet have a high height. These computations provide approximate dimensions for fabrication of rings that display the different magnetic states.

The clockwise and anticlockwise vortex states of ferromagnetic rings have been proposed as bit representations in future ring based magnetic storage media. In symmetric rings, the two vortex states are equally likely. In addition, symmetric rings in the vortex state have no magnetostatic energy. Measurement techniques sensitive to the magnetic field gradient from a sample such as magnetic force microscopy cannot measure the vortex chirality in symmetric nanorings.

Saitoh et al. demonstrate the control of vortex chirality in ferromagnetic nanorings by introducing asymmetry [18]. In this paper, a decentered ellipse forms the inner hole of a permalloy ($Ni_{81}Fe_{19}$) nanoring. The rings have an outer diameter of 500nm and are 20nm thick. The decentered ellipse has a major axis of 250nm and a minor axis of 150nm and it is offset by 50nm
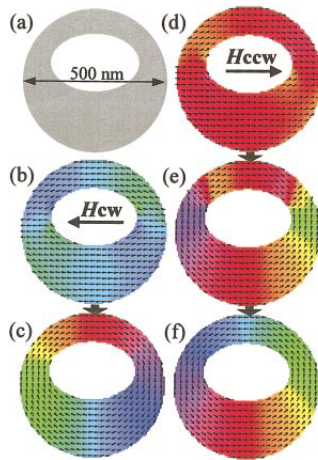
Figure 2.12: Micromagnetic simulations that follow the solution of the Landau-Lifshitz equation on a two dimensional grid of the ring shown in (a) demonstrate how a field to the left(b) will cause domain wall annihilations at the narrowest ring width leading to the clockwise vortex observed in (c). Similarly, the rightward field(d) leads to the counterclockwise vortex chirality shown in (f). [18]

from the center of the ring. Magnetic simulations show dipole states in a high external field form onion states as the applied field becomes weaker. The gradient of domain wall energy controls the movement of domain walls. Annihilation of domain walls occurs at the narrowest ring width when the applied field is along the asymmetric axis of the ring as illustrated in Figure 2.12. In addition, there is a divergence in the magnetization of the vortex state in asymmetric rings that is detected through MFM unlike in symmetric rings where the vortex state is a stray field−free state. The vortex chirality affects the direction of divergence. Figure 2.13 presents simulation and MFM results that distinguish the clockwise chirality from the counter clockwise chirality in asymmetric rings.
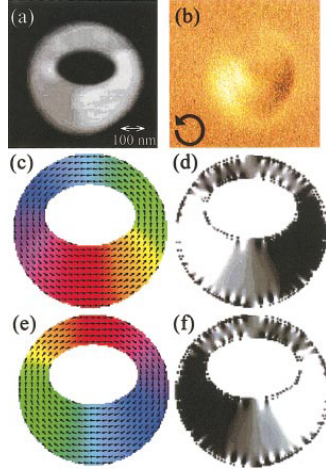
Figure 2.13: (a) The atomic force image of a $Ni_{81}Fe_{19}$ ring with an outer diameter of 500nm and a thickness of 20nm. The inner hole is an ellipse with a major axis 250nm, a minor axis 150nm that is decentered 50nm from the center of the ring. (b) A magnetic force image of the magnetization of the ring. (c) The magnetic moment distribution of the ring in the counterclockwise chirality. (d) Simulation following the Landau Lifshitz equation showing the divergence of the magnetic moments in the ring. (e) Magnetic moment distribution in the clockwise chirality. (f) Simulation of the divergence of magnetic moment distribution in the clockwise chirality. [18]

The paper by Saitoh et. al. demonstrates the control of vortex chirality in asymmetric rings by applying an external field along the asymmetric axis. We are exploring a novel technique of controlling chirality in magnetic ring structures using a current generated field positioned at the center of a ring. This magnetic field decays with distance from the center of the ring and the magnetic field lines curl around the ring circumference as dictated by the right hand rule. This mechanism offers additional flexibility in that chirality can be controlled in symmetric and asymmetric rings at reasonable current densities

as will be explained in Section 4.3.

Chapter 3

Fabrication

We fabricate Permalloy (FeNi) nanorings to explore the in-plane magnetic configurations of nanorings as well as to demonstrate manipulation of vortex chirality using an Oersted field. During fabrication, we use electron beam lithography to pattern the resist layer. We then deposit magnetic material onto the patterned resist by electron beam evaporation. In the final step, we use acetone to lift-off the resist layer. In this chapter, we review the fabrication procedure in detail. A lot of effort is dedicated to perfecting the fabrication technique. Sample defects significantly alter the magnetic properties of magnetic nanostructures.

3.1 Substrate Cleaning

Our sample substrate is a 200μm thick silicon wafer. Fabrication begins with cleaning the wafer. The wafer is rinsed in deionized water before chemical cleaning. Chemical cleaning involves three different solutions used in the following sequence:

1. 5 minute soak in Trichloroethylene with ultrasonic shaking

2. 5 minute soak in Acetone with ultrasonic shaking

3. 5 minute soak in Methanol with ultrasonic shaking

4. 1 minute dry off with Nitrogen (N_2)

Methanol cleaning is performed last because methanol evaporates quickly carrying with it any solutions on the surface of the substrate. We show the side view of our sample at each fabrication stage. At this point, we have a clean silicon sample substrate shown in Figure 3.1.

Figure 3.1: Silicon substrate

3.2 Evaporation

One of our experimental goals is to manipulate nanoring chirality using an Oersted field. For this purpose, we need a conducting sample substrate layer. We deposit a thin gold layer onto the sample substrate through thermal evaporation. In this process, the source gold is heated by a filament in a vacuum. Evaporated gold atoms travel easily in the vacuum condensing on the cold silicon wafer located above the source material as shown by Figure 3.2. In our set up, evaporated gold atoms travel with minimal resistance onto the substrate in low vacuum levels of about 10^{-6} torr. During evaporation, resistive heating of a filament causes gold evaporation. The thickness of the deposited film depends on evaporation time; for a thin layer we evaporate gold
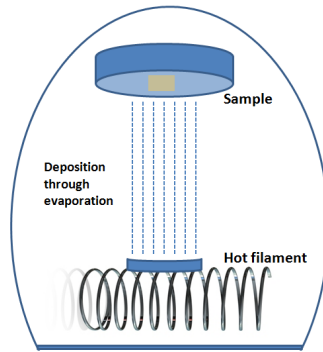
Figure 3.2: Schematic of thermal evaporation where the source material is heated by a filament in a vacuum condensing on the sample surface above the source material.

onto the substrate for about 60 seconds. At this stage, our sample looks as shown in Figure 3.3.

Silicon

Figure 3.3: Sample substrate after the evaporation of a 20nm layer of gold

3.3 Resist

Electron beam resists are polymers sensitive to electron exposure . Resists assist in pattern transfer and they are deposited on the sample surface through spin coating. A mask developed using the computer aided design system defines regions of resist exposure that will yield the desired sample pattern. An electron beam breaks up the polymer chains on the exposed regions. There are two kinds of resist: positive resist and negative resist. In

positive resists, polymer chains are broken during exposure becoming soluble in developing solutions. On the other hand, electron exposure strengthens the polymer chains in negative resists making the exposed regions less soluble in developing solutions. We are using positive resists. During electron beam lithography (EBL), collisions between the electrons and polymer atoms weaken the resist layer in a process called scattering. Some electrons are reflected back onto resist layer by the substrate contributing to more collisions between polymer and the electrons in a process known as back scattering [20].

We are using a bilayer of positive resist. The first polymer layer is methyl methacrylate (MMA). The second polymer layer is polymethyl methacrylate (PMMA), which has a higher molecular weight [20] than MMA. These polymers occur in powder foam and they dissolve in chlorobenzene or anisole. PMMA degrades much less than the MMA layer during ebeam lithography. This creates an undercut (Figure 3.4) in the exposed regions which makes lift-off much easier. The thickness of the resist layer depends on polymer concentration and the spin coating speed. The sensitivity of the resist layer, electron scattering, as well as the proximity of pattern features affects writing resolution (Section 3.4). Resist sensitivity refers to how much the polymer degrades for a given ebeam exposure. Resist that degrades the least for a given exposure yields the highest resolution [20]. Closely spaced sample features can decrease the resolution of resist because the resist layer between very close features can be weakened during exposure.

We deposit the polymer in solution form on the substrate and spin the substrate at 4500 revolutions per minute (RPM) for 60 seconds, creating a thin resist layer. Resist film thickness uniformity is important for pattern formation. MMA is deposited first, followed by 7 minutes of baking at 180° to increase polymer adhesion and to dry the deposited polymer. Soon after,

46

Figure 3.4: a) Bilayer resist deposition onto the sample b) The resulting undercut in the bilayer after ebeam exposure and development is due to the lower molecular weight of the MMA layer in comparison to the PMMA layer

PMMA is deposited and baked following a similar procedure. A side view of the sample after resist deposition and E-beam lithography is shown in Figure 3.4.

3.4   Electron beam lithography(EBL)

During EBL, a high energy electron beam transfers the design pattern onto the resist bilayer by weakening exposed polymer regions. We use a thermal field effect scanning electron microscope (JEOL JSM$-$7001F FE SEM) to perform lithography and to image the fabricated structures. EBL begins with pattern design facilitated by the Nabity Nanometer Pattern Generation System (NPGS), which is built into the SEM interface. The smallest feature size and the density of features are important considerations during pattern design. The smallest feature sizes should be of the same length as the narrowest lines a given SEM can write. Sample density should account for the back scattering effect that weakens a large area of the resist surrounding a written structure.

The pattern defines the regions of polymer exposure to create the desired sample structures. Ebeam writing can be done either by vector or raster

Figure 3.5: A picture of the JSM-7001F Field emission scanning electron microscope (FESEM)

writing. Raster writing involves scanning the entire sample surface line by line while blanking the beam as needed ensuring that only exposure regions receive the beam. In vector writing, the beam is moved about the surface scanning only the regions to be exposed. The vector writing technique is commonly used and in some cases this does not require a beam blanker since insignificant exposure occurs as the beam moves from one region of exposure to the next one. Vector writing also gives higher writing speeds since only exposed regions are scanned. Our SEM uses vector writing; however, it also provides a beam blanker to protect unwritten resist regions from exposure. Beam blankers should have a fast repetition rate and very short rise/fall times. In general, writing speeds depend on resist sensitivity, the beam current and the maximum beam movement speed of a given SEM.

It is important that the lithography coordinate system is well aligned

with the writing field to correctly position the sample on the substrate. This is attained by imaging the writing field and then registering the lithography coordinate system with marks on the sample [20]. The field size is the approximate area where a sample pattern is to be written. The size of the writing field depends on the magnification of the SEM. Fine features can be written in field sizes of about $50 \times 50 \ \mu m^2$ to $200 \times 200 \ \mu m^2$. The size of the smallest feature sizes depends on the resistivity of the resist layer as well as the optimization of the microscope. Using the (JEOL JSM$-$7001F FE SEM), line widths as small as 25 nm have been achieved.

The distance from the ebeam source to the sample is known as the working distance. This distance determines the smallest spot size that can be written and the magnification settings. A short working distance gives a higher resolution. The range of approximate working distance is about 5 to 10 mm. We use a working distance of 8mm. The electron beam's accelerating voltage affects the depth of beam penetration. High accelerating voltages give much deeper penetration limiting the number of scattered electrons thus resulting in finer features. We use a high accelerating voltage of 30 kV which writes fine lines. Low beam currents give smaller spot sizes on the sample. The smallest spot sizes occur when we use high accelerating voltages and low beam current values. The current range for a FE SEM is 10$-$20 pA.

Other important microscope optimizations include the focus and astigmatism. These parameters are optimized by repeatedly focusing and optimizing the astigmatism beginning from a low magnification to a high magnification. Also important is the ebeam aperture centering also known as the wobble. Our SEM provides an SEM user interface which displays important SEM parameters and automates many user adjustments. In our experiment, our design pattern is an array of rings of varied ring sizes. When writing nar-

rower rings, we use line dosage where closely spaced fine lines are written to create the ring structure while we use area dosage for wider rings. Development follows ebeam lithography. At this stage, the sample is immersed in a developing agent for 60 seconds where the broken polymer chains are dissolved. We use methyl isobutyl ketone (MIBK) as our developing agent. Development over long periods could wash away the unbroken polymer chains destroying the pattern. The sample is then rinsed and dried by blowing it with nitrogen gas.
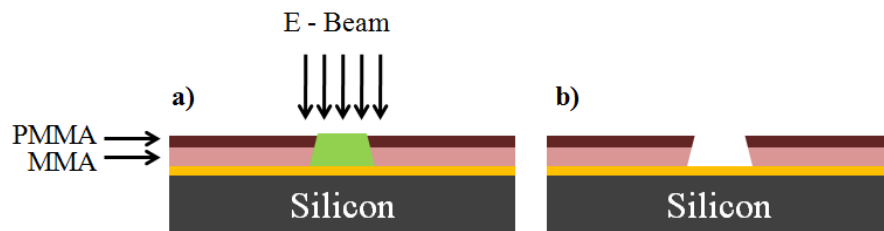
Figure 3.6: a) Bilayer resist exposed to an electron beam. The green region shows the broken polymer chains. b) The developed sample illustrating the removal of the broken polymer chains.

3.5 Material Deposition

Our samples are made of permalloy. We deposit the sample materials through either sputtering or ebeam evaporation. The two deposition methods differ in the control of the direction of the deposited material [20]. Sputtering disperses the deposit particles over wide angles. As a result, structures of non-uniform thickness are formed because of the wide angle of deposition that may randomly favor deposition in some sample areas in comparison to others. Deposition is collimated in the ebeam evaporation process and material

deposits only on the directly exposed regions as is illustrated in Subsection 3.5.2. Evaporation gives the best results during lift-off. Lift-off is the process of removing the resist layer leaving only the sample material on the substrate. Both of these deposition techniques must be carried out in ultra high vacuum to ensure that deposition is successful. Table 3.1 relates the pressure in the deposition chamber to the mean free path illustrating a longer free path for deposition materials in high vacuum environments.

Table 3.1: Mean free path as a function of pressure [21]

Pressure (Torr)	Mean free path (cm)
10^1	0.5
10^{-4}	51
10^{-5}	510
10^{-7}	5.1×10^4
10^{-9}	5.1×10^6

3.5.1 Sputter Deposition

Sputtering is the deposition technique where a plasma beam hits the target material ejecting target atoms that travel at high velocities over wide angles. The ejected target atoms form a layer on the entire sample surface. Sputtering deposits materials on the resist wall edges making lift-off difficult. This process occurs in a vacuum. We use the AJA international Orion 8 sputtering system with load lock chamber (Figure 3.7.(b)). Although sputtering produces rugged sample edges after lift-off, it creates uniform films because it is a cold deposition process. The deposition time affects the thickness of the structures with longer times yielding thicker films.
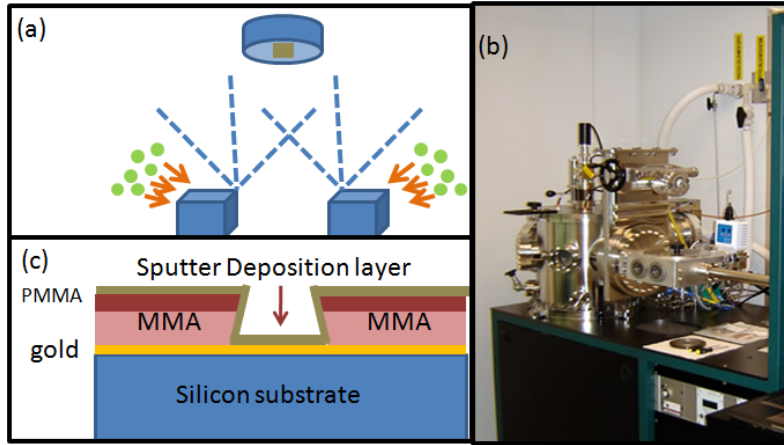
Figure 3.7: (a) An illustration of the sputtering process where energized argon atoms break off permalloy atoms from the target, spreading them in all directions, depositing a thin permalloy film on the sample located above the target material. (b) A picture of the AJA international Orion 8 sputtering system with load lock. (c) The deposition on the sample resulting from sputtering.

3.5.2 Ebeam Evaporation

In this deposition process, a high intensity electron beam gun with energies of about $3-20$keV is focused on the target material. The electrons locally heat the material causing target evaporation. The source material is placed on a water cooled hearth. A magnetic field is used to focus the electron beam. The coolant prevents chemical reactions by lowering the source temperature, thus decreasing the probability of source contamination[21]. Electron beam evaporation gives high deposition rates of about 50 - 500 nm/minute and ensures uniform film thickness reducing rugged sample edges. The main disadvantage of e-beam evaporation is radiation. The electron beam produces X-rays that can damage the sample and affect the experimentalist.
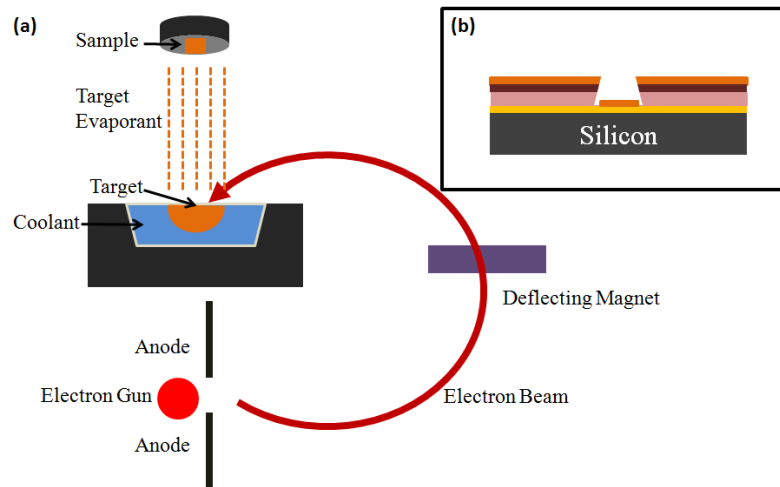
Figure 3.8: (a) Ebeam evaporation process, which involves high energy electrons bombarding the source material causing evaporation (b) The side view of the sample after material deposition. This deposition process does not coat the resist wall edges simplifying the lift-off process.

3.6 Lift-off

The final fabrication procedure involves dissolving the resist layer leaving only the deposited target material on the sample surface. This process is called lift-off. The solvent for PMMA and MMA is acetone. The sample is soaked in acetone for 12 hours. Deposition procedures that do not coat the resist walls give the best results during lift-off. A thin layer of platinum is deposited on the sample surface to protect it from oxidation through ebeam evaporation.
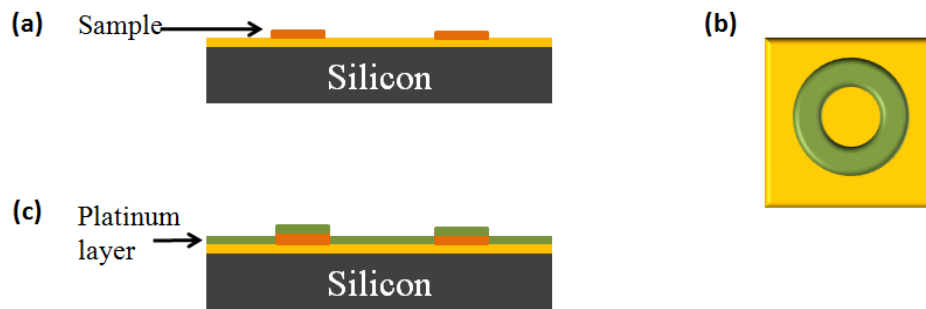
Figure 3.9: (a) A side view of the sample after lift-off. (b) The top view of the sample following lift-off showing the ring geometry. (c) A side view of the sample after the deposition of the protective platinum layer

Chapter 4

Characterization

We need imaging techniques with nanometer resolution to characterize magnetic nanorings. Scanning probe microscopy has a resolution ranging from 100μm to 10pm [22]. We are using scanning probe techniques to examine the topography and magnetizations of nanoring structures. In this chapter, we describe the characterization techniques used and the experimental implementation of the Oersted field.

4.1   Atomic Force Microscopy (AFM)

AFM is an imaging technique where the forces between a sharp tip and a sample surface are measured to determine the surface topography. An AFM uses a tip with an end curvature of a few nanometers that is mounted on one end of a Silicon cantilever. The tip is scanned across the surface allowing tip-sample forces described by Hooke's law to change the dynamic properties of the tip. A laser that reflects off the top of the cantilever onto a position sensitive photodiode tracks changes in tip properties as shown in Figure 4.1.

Feedback mechanisms maintain the initial probe settings throughout a scan. The sample is mounted on a piezo that moves along the Z axis as controlled by the feedback system to ensure a constant tip-sample separation. The size of a piezo electric material depends on the applied voltage across the material. The changes in the properties of the tip during a scan are used to derive the height information of a sample as a function of the sample's X and Y positions [22]. The tip geometry affects resolution; the topographic image is a convolution of the tip and the sample surface as shown in Figure 4.1 b.
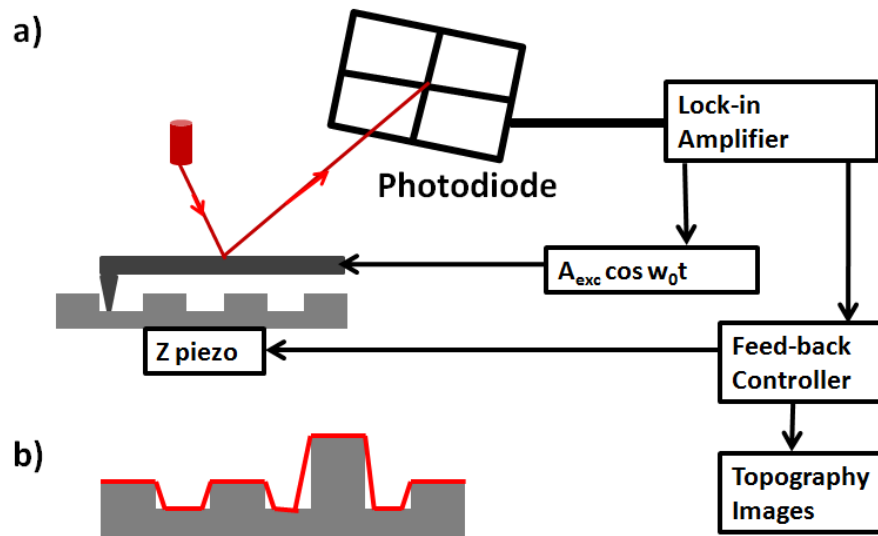
Figure 4.1: a) Illustration of atomic force microscope operational set-up. b) The image is a convolution of the tip and the sample surface. The red line shows the resulting height image

AFM is performed in two common modes, contact mode and tapping mode. In contact mode, the tip is dragged along the sample surface. During the scan, the AFM ensures a constant cantilever deflection by appropriately moving the stage along the Z direction. A plot of the stage motion along the Z axis as a function of sample position yields a topographic image of the sample.

This technique is not suitable for delicate samples because the tip exerts a dragging force on all sample areas during imaging.

In tapping mode, the cantilever is oscillated at its resonant frequency. Tip-sample force interactions alter the dynamic properties of the tip such as amplitude, phase and resonant frequency. We can measure sample characteristics from the changes in the oscillation properties of the tip. In this imaging mode, the AFM tip is modeled as a simple harmonic oscillator. The force gradient in the direction of oscillation of the tip alters the effective spring constant of the tip as indicated in Equation 4.1. k is the intrinsic spring constant, F is the magnetic force on the cantilever.

$$k_{eff} = k - \frac{\partial F}{\partial Z} \tag{4.1}$$

Repulsive forces increase the effective spring constant while attractive forces decrease the effective spring constant. Variations in the effective spring constant alter the resonant frequency of the cantilever as indicated in Equation 4.2 and 4.3.

$$w_\circ = \sqrt{\frac{k}{m}} \tag{4.2}$$

$$w = \sqrt{\frac{k_{eff}}{m}} \tag{4.3}$$

The mass of the cantilever is given by m, the resonant frequency is $w_\circ$ and the altered resonant frequency is ω. Replacing Equation 4.1 in Equation 4.3, we obtain:

$$w = \sqrt{\frac{k - \frac{\partial F}{\partial Z}}{m}} = w_\circ \sqrt{1 - \frac{\frac{\partial F}{\partial Z}}{k}} \tag{4.4}$$

Following the binomial theorem for small force gradients relative to the spring constant Equation 4.4 is approximated as:

$$w = w_\circ (1 - \frac{\partial F}{2k\partial Z}) \tag{4.5}$$

The change in resonant frequency is given by:

$$\delta w = w_\circ - w = -\frac{\partial F}{2k \partial Z} \tag{4.6}$$
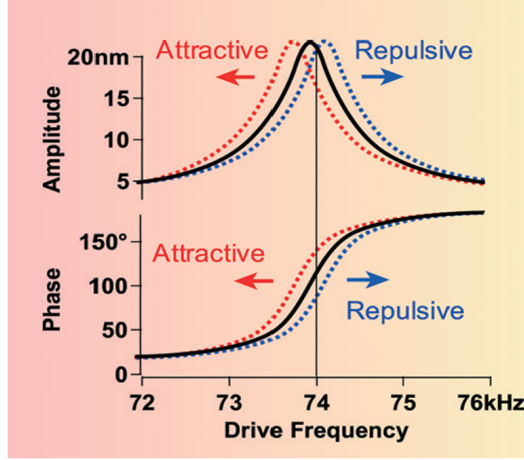
Figure 4.2: Probe-sample forces shift the cantilever's resonant curve. Attractive forces shift the curve left while repulsive forces shift the curve to the right. The phase plots show an increase in phase when the forces are attractive and a decrease in phase for repulsive forces [23].

A repulsive force will increase the resonant frequency while an attractive force will decrease the resonant frequency. The cantilever behaves like a simple harmonic oscillator where the phase and amplitude depend on the resonant frequency. The phase of a cantilever oscillated at a frequency other than the resonant frequency is:

$$\theta = tan^{-1} \frac{ww_\circ}{Q(w^2 - w_\circ^2)} \tag{4.7}$$

Q is the quality factor of the cantilever. The change in phase as one is imaging a magnetic surface is given by [24]:

$$\frac{\delta \theta}{\delta w} = [\frac{\partial \theta}{\partial w}]_{w_\circ} \tag{4.8}$$

58

The above mathematical descriptions help us to understand how tip-sample forces change the dynamic properties of the tip and in turn how the changes in the tip dynamic properties allow us to measure the sample topography. A more qualitative illustration of AFM is given in Figure 4.3. The image contrast gives us the height information of the sample. We are using the MFP3D atomic force microscope built by Asylum Research.

Figure 4.3: Height profile of a sample and the resulting AFM contrast. High features have a lighter contrast as compared to lower features

4.2 Magnetic Force Microscopy

Magnetic force microscopy (MFM) is an imaging technique sensitive to the long range magnetic forces between a magnetic probe and a magnetic sample. During MFM, an image of sample magnetization is obtained by measuring the force gradient between a magnetic tip and the out of plane stray field of a magnetic sample. MFM is an important characterization tool that requires no sample preparation, can be performed in a variety of environments and has a high resolution. MFM probes consist of a flexible cantilever with a sub - micron tip coated with a magnetic layer. MFM occurs in two scans. The topographic scan, which is performed first, records the height of surface features while the MFM scan lifts the probe a few nanometers above the surface

enabling tip deflections as a result of magnetic interactions between the tip and the sample. As a result, we can correlate magnetic states to the geometry of individual ferromagnetic nanoparticles.

The topographic scan is usually performed in tapping mode as described in Section 4.1. An MFM scan follows the topographic scan. During MFM, magnetic tip-sample interactions change the effective spring constant with attractive forces shifting the resonant curve left and repulsive forces shifting the resonant curve right. The polarization of the tips affects the direction of the tip-sample force gradient. The gradient is negative when it is polarized in the same direction as the sample surface while it is positive when the tip is polarized in the opposite direction to the surface.
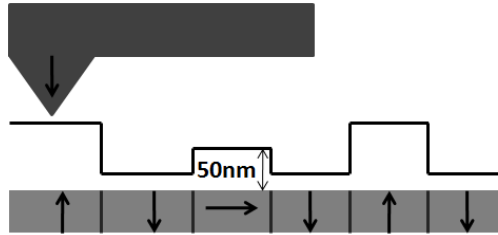
Figure 4.4: Tip-sample interactions during MFM

Sample-probe distances in between 10nm - 200nm will detect tip deflections as a result of magnetic interactions between the sample and the tip. The standard MFM probes we use are made of a silicon cantilever coated with cobalt chromium. MFM tips are specialized for different imaging purposes. High coercivity tips have high switching fields, hence they retain their magnetization throughout a scan. On the other hand, low coercivity tips display unstable magnetization. A stronger magnetic signal is observed when imaging with high moment tips, which have more magnetic material contributing to stronger interactions with a magnetic sample. Although high moment tips give

a large signal, they can alter the magnetization of the sample. Low moment tips image the magnetic domains of a sample without affecting the sample magnetization.

Table 4.1: Magnetic tip classifications of Silicon cantilevers[25]

Probe	Tip radius	Coating material	Coercivity (Gauss)
Standard	30nm	50nm Cobalt Chromium	300 - 400
Low Coercivity	20nm	30nm Permalloy	< 100
High Coercivity	30nm	Cobalt platinum and iron platinum	> 5000
Low Moment	12nm	15 nm Cobalt Chromium	300 - 450
High Moment	50nm	100nm Cobalt Chromium	500 - 600

MFM results are qualitative because quantization of MFM results is difficult due to the complex force interactions between the sample and the tip that depend on tip geometry, tip magnetization, sample magnetization, nature of the sample, tip-sample distance and the external field. Although we cannot quantize MFM results, they are a true reflection of the magnetization of a structure. A simulation of the divergence of the stray field from a magnetic structure helps us to relate magnetic contrast to magnetization. Figure 4.5 is a simulation by Abby Goldman that shows dipole configuration in a bar magnet with a diverging stray field at the ends of the magnet. The contrast image shows the strength and the direction the diverging field. When the magnetic moments are facing upward, the diverging field is out of the plane which correspond to a dark contrast and when the field moves into the plane the contrast is lighter. During MFM, a change in the tip dynamic properties occurs due to the force interactions between the diverging field of the probe and that of the sample. This simulation illustrates how we can relate MFM

contrast to the sample magnetization.
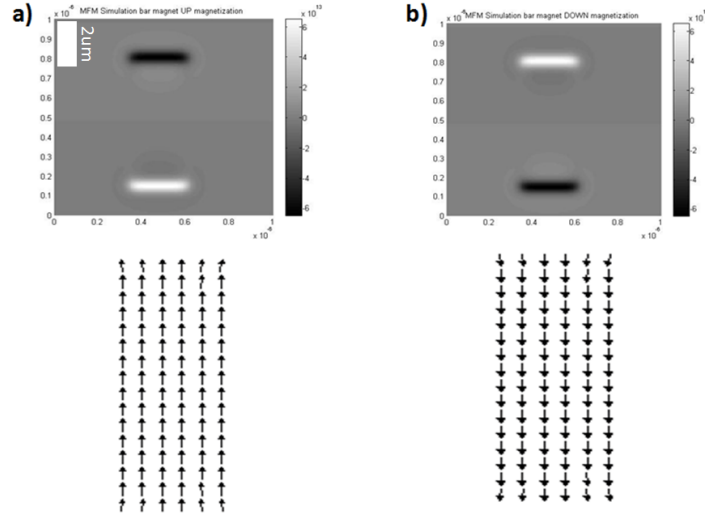
Figure 4.5: An illustration of how magnetization relates to MFM contrast. A diverging field out of the bar magnet corresponding to a dark contrast while a diverging field into the bar magnet gives a darker contrast. In the actual implementation of MFM the contrast depends on sample and tip magnetizations

4.2.1 Variable Field Module (VFM)

We are studying nanoring configurations as a function of the in-plane field. The variable field module of the AFM generates different in-plane fields using an earth magnet. The earth magnet is rotated 360° varying the field. We have observed that the VFM gives fields in the range of $\pm$ 2900 Gauss and a resolution of about 5 Gauss. We mount the sample on top of the VFM. The sample is exposed to a slightly weaker field depending on sample thickness than that generated by the VFM. Earth magnets eliminate problems such as heating that would be observed if the field was generated by a solenoid. The

main problem we face when using the VFM is sample drift caused by vibrations of the motor as it rotates the magnet creating different fields. Figure 4.6 shows the VFM set-up.
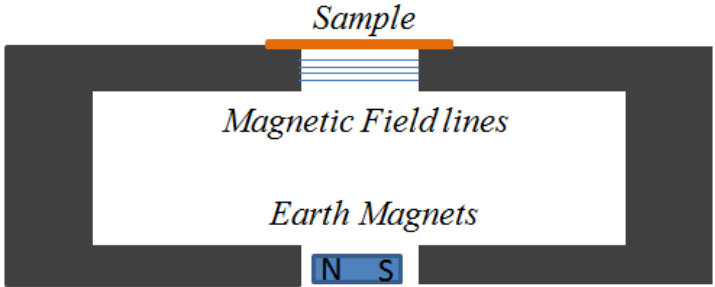
Figure 4.6: An illustration of the VFM set-up.

4.3 Oersted Field

The vortex state is the preferred state in ring structures because of its low energy that results from eliminating energy contributions from magnetostatic energy and minimizing the local exchange energy between adjacent moments since these moments are almost parallel. The vortex state, which appears in two forms, the clockwise and counterclockwise vortex, has potential applications in memory. However, creating and measuring the vortex chirality is a challenge [26]. Understanding the switching mechanisms into the vortex is important for controlling this configuration in future applications. We present a new method of controlling vortex chirality using the Oersted field from a conducting AFM tip that approximates the field from an infinite conducting wire placed at the center of the ring. MFM is then be used to image the magnetization of the ring after applying an Oersted field. We can image the vortex chirality in asymmetric rings using MFM.

63

Control of chirality has been implemented in asymmetric rings where domain wall annihilation leads to the vortex state. Vortex formation involves the annihilation of two domain walls whose movement is controlled by the energy of the domain wall. Minimization of energy causes domain wall motion to the narrowest ring width. This process is facilitated by an in-plane field applied along the asymmetric axis of the ring. The Oersted field is a direct way of controlling switching between two vortex configurations. However, we note that magnetization reversal in nanoring structures is complicated because the structure lacks an end surface that assists in the nucleation of a domain wall [26]. Domain wall formation involves the nucleation of two domain walls at two locations of the ring and this process involves a high cost in energy.

Interesting switching mechanisms in rings in an Oersted field have been observed in simulations performed by Abby Goldman using the public domain simulation program OOMMF [5]. In these simulations, the Oersted field is a spatially non-uniform field in a distribution similar to that of an infinitely conducting wire placed at the center of a ring. The current is increased from a negative to a positive value generating a hysteresis showing ring vorticity at different current values. Vorticity is defined by Equation 4.9. A is the area of the ring, $\mathbf{r}$ is a unit vector in the radial direction and $\mathbf{M}$ is the magnetization vector at that point. The equations tells us that the magnitude of vorticity is greatest when the $\mathbf{r}$ and $\mathbf{M}$ are perpendicular and this is when the ring is in the clockwise or counterclockwise vortex.

$$V = -\frac{1}{A} \int_A (\mathbf{r} \times \mathbf{M}) \cdot \mathbf{dA} \tag{4.9}$$

Simulations have predicted switching between vortices in a permalloy ring with a thickness of 5nm. Switching is mediated by an experimentally attainable current of 5mA. 360° domain walls unpeal in the switching process

64
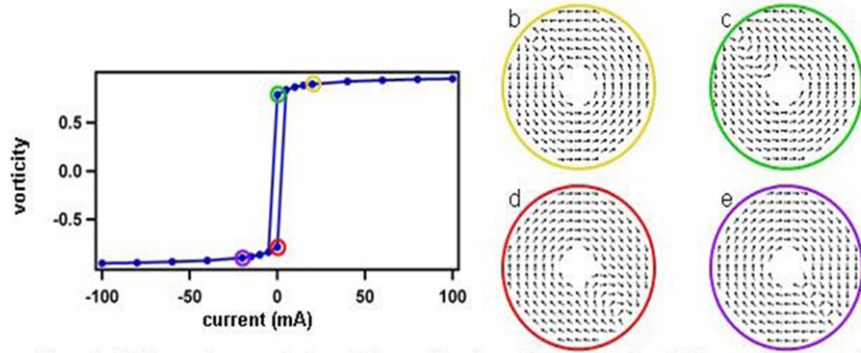
Figure 4.7: A hysteresis of a 5nm thick permalloy ring with an outer radius of 400nm and an inner radius of 100nm simulated by Abby Goldman. Current values as low as 5mA are observed to cause state transitions from one vortex chirality to the other. Switching between chiralities using a decreasing current involves a 360° domain wall (b) that widens (c) before forming a clockwise vortex defined as having -1 vorticity. When the current is increasing the 360° domain wall unpeals and forming another 360° domain wall with the opposite chirality (e) this domain wall widens (d) before forming the counterclockwise vortex that has a vorticity of 1

as shown in Figure 4.7. Simulation results have been used to approximate ring dimensions for experiment as well as to determine target current values estimated to induce switching. We expect high switching fields in smaller narrower rings where magnetization reversal involves a large rotation of adjacent moments leading to high energy costs. Thinner rings have lower switching fields because there are fewer magnetic moments to be switched during magnetization reversal thus requiring less energy. High switching fields demand high current densities which will possibly melt the metal coating of standard silicon cantilevers. We are using solid metal tips which have a bigger tip radius. This reduces our imaging resolution. However, using these tips we are

able to pass currents as high as 10mA without completely damaging the tip
[26].

Chapter 5

Results and Discussion

In this chapter, we present and discuss fabrication and characterization results.

5.1 Fabrication results

We have fabricated arrays of nanorings with different geometries to investigate the stability of magnetic configurations in these different geometries. Permalloy rings are fabricated through electron beam lithography followed by lift-off. A resist bilayer of PMMA and MMA is deposited onto a silicon wafer. Narrow rings as shown in Figure 5.1.a) are written using line dosage. Dosage refers to the amount of charge per unit area. When writing ring structures using line dosage, the SEM writes concentric circles that are a few nanometers wide and have increasing diameters beginning from the inner diameter of the ring moving outwards to the outer diameter of the ring. Line dosage gives a better resolution when writing narrow rings. Wider rings as shown in Figure 5.1.b) are written using area dosage where a large area is exposed to the beam during writing.

The rings are imaged in tapping mode atomic force microscopy using the Asylum research MFP3D AFM. Tapping mode is gentle on a sample because the tip oscillates while tapping the surface unlike contact mode where the tip drags along the surface.
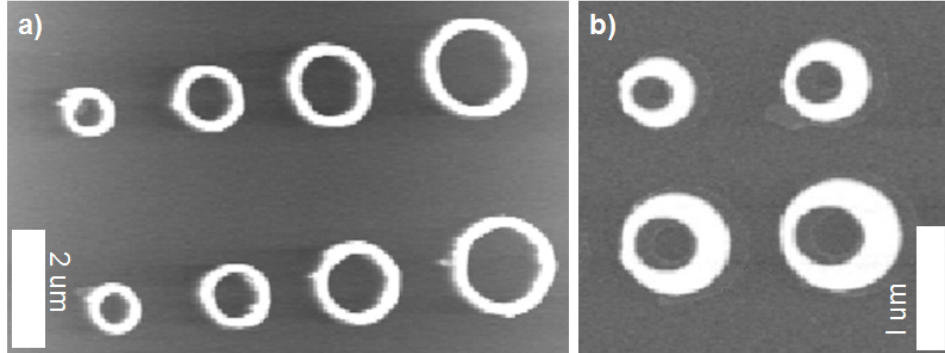
Figure 5.1: Atomic force microscope images of permalloy nanorings arrays. a) An array of narrow rings with a thickness of 25nm. The outer diameter ranges from 0.86um to 1.58um. The ratio of the inner diameter to the outer diameter is ≈ 0.5 b) An array of asymmetric rings ≈ 30nm high with an outer diameter ranging from ≈ 1 um to 0.53um. The inner hole is made of an ellipse decentered from the center of the ring.

5.2   Magnetic Force Microscopy(MFM)

We are implementing MFM in a changing in-plane field to understand the switching mechanisms as well as the size dependent stability of magnetization in nanoring structures. During MFM, we raise the tip about 20nm above the sample and decrease the probe's amplitude of oscillation to avoid striking the sample surface. We begin by imaging a hard drive sample to ensure that our probe is magnetized before imaging magnetic nanorings. Here we introduce the

main configurations we have observed through MFM and discuss the balance of magnetic energy that results in the different states. The dipole state is
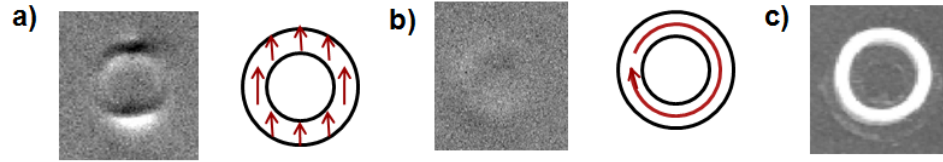
Figure 5.2: An illustration of MFM magnetization and the magnetic moment alignment of the different states. (a). Shows the dipole state observed at high external fields (b) Shows the vortex state which is observed at low external fields (c) the AFM image of the nanoring

stable at high field values. Figure 5.2.a) is an MFM image of a symmetric ring in the dipole state at -2000 gauss. The ring has an outer diameter of 1.08 μm, an inner diameter of 0.58 μm and a thickness of 25nm. We observe the dipole state when the sample is exposed to high external field values that align the magnetic moments in the direction of the applied field. In this state exchange energy is very low because moments are parallel with one another. However, there is a high cost in magnetostatic energy because of the large stray fields from the poles of the dipole state.

At lower field values we observe the vortex state where the magnetic moments curl around the circumference of the ring. In this state there is no magnetostatic energy and exchange energy is locally minimized because adjacent moments are close to being parallel. Figure 5.2.b) shows the ring in the vortex state. The vortex state was observed at 0 gauss.

5.2.1   Ring hysteresis

The behavior of a magnetic structure in a changing magnetic field is well described using a hysteresis curve. A simulation by Abbey Litch shows the expected hysteresis in nanoring structures. When we initialize at a negative field, in our case this is at -400 Gauss, the rings are in dipole state which has a magnetization of -1 as shown in Figure 5.3. As the field is progressively increased, we get to a switching field where there is a big increase in magnetization from ≈ -0.8 to 0. This switching field as shown in Figure 5.3 is about 20 Gauss. This is a transition from the dipole state to the vortex state, which involves the annihilation of two domain walls forming the single domain vortex state that has zero magnetization.
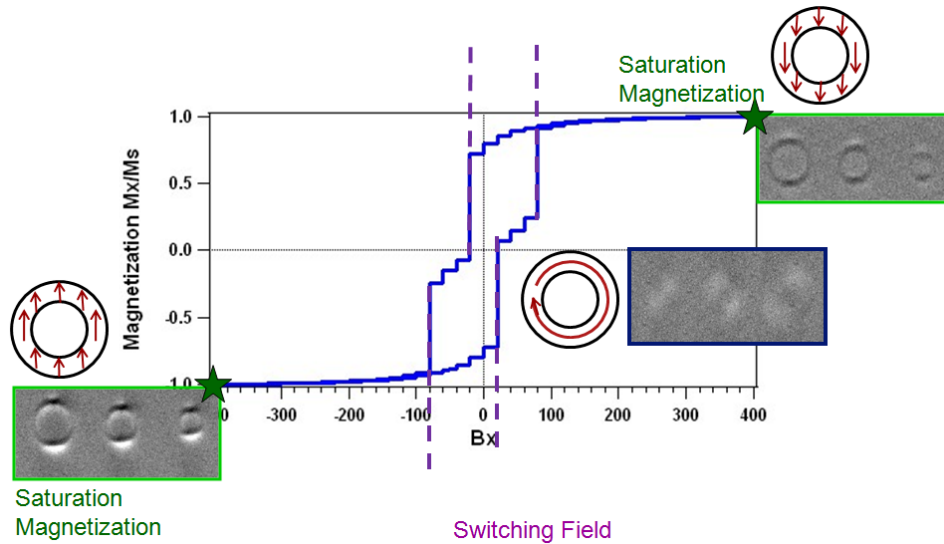

Figure 5.3: The simulated hysteresis curve of a nanoring structure. The MFM images at different magnetization states are also presented

As we further increase the field we encounter another switching field at 100G where the magnetization changes from ≈ 0.3 to ≈ 0.9. This is a

transition from the vortex state to the dipole state through the nucleation of two domain walls. This dipole state has the opposite polarity to that of the dipole state observed at negative fields. Saturation is attained at $\approx$ 350 Gauss. To complete the hysteresis we decrease the field progressively. There is a switching field at $\approx$ -20 Gauss, where we observe a decrease in magnetization from $\approx$ 0.7 to $\approx$ -0.1. This is a transition from a dipole state to a vortex state through the annihilation of the two domain walls present in the dipole state. On further decreasing the field we find another switching field at $\approx$ -80 Gauss where two domain walls are nucleated forming the dipole state with a magnetization of $\approx$ -0.9. Magnetic saturation occurs at $\approx$ -300G. This completes our hysteresis curve.

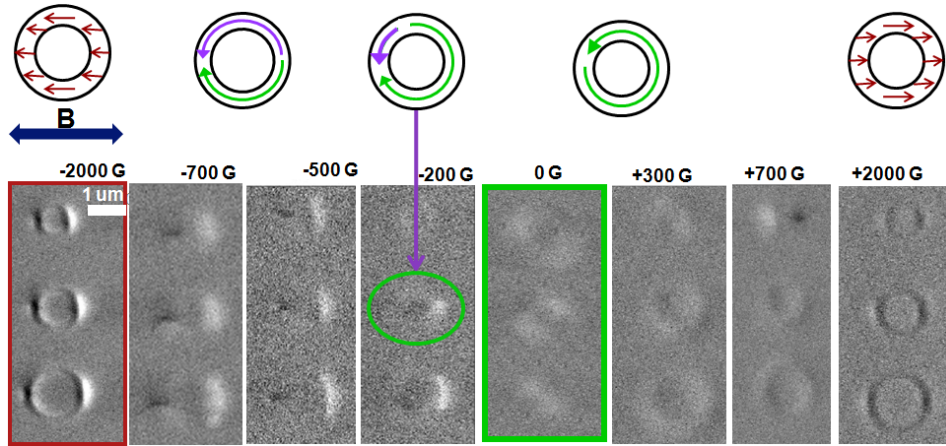Figure 5.4: MFM images of three rings with uniform ring widths but with different diameters in an increasing external in-plane field.

Experimentally, we have examined magnetic state evolution in an increasing field beginning from -2000 Gauss to 2000 Gauss observing a similar pattern as that shown by the simulation. Figure 5.4 shows MFM images of three rings of uniform ring width but different diameter in an increasing mag-

netic field. We begin with a field of -2000G where all the rings are in the dipole state. Upon increasing the field, we observe transitions into the vortex state at -200 Gauss. Figure 5.4 shows domain wall annihilation illustrated by the light and dark contrast appearing close to one another at -200G. At 0 gauss all the rings are in the vortex state.
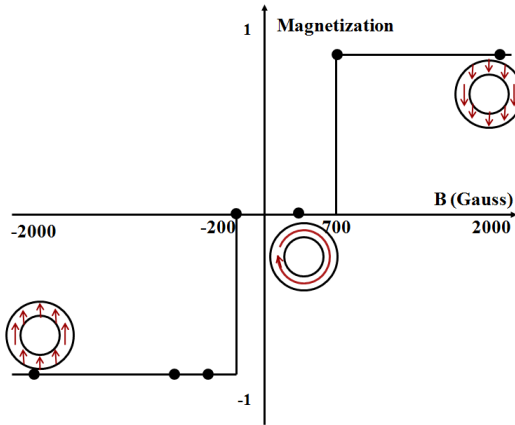
Figure 5.5: A qualitative 1/2 hysteresis of our MFM results shown in Figure 5.4. We initialize at a negative field of -2000G where the ring is in the dipole state and increase the field progressively. At -200G we switch into the vortex state which remains stable until 700G when we switch into the opposite dipole state.

The vortex state persists until the field gets to 700 gauss where two domain walls are nucleated in the smallest ring. This begins the transition from the vortex state to the dipole state at high field values. At 2000G, all the rings are in the dipole state. We observe a decrease in magnetic contrast in Figure 5.4 from our first scan at -2000G to our last scan at 2000G. One possible explanation for the progressively weakening contrast is a that the probe is progressively losing its magnetization as we image the sample. We present a qualitative 1/2 hysteresis curve of our experimental results in Figure

5.5. We define all dipole states as having a magnetization of $\pm$ 1 depending on the field direction. Negative fields yield a magnetization of -1 for the dipole state while positive fields give a magnetization of 1 for the dipole state. The vortex state is defined as having a magnetization of 0.

5.2.2   Stability Dependence on Ring Diameter

We would like to understand how ring geometry affects the stability of different ring magnetizations. One of the aspects we have examined is ring diameter. Figure 5.6 shows three rings of different outer diameter but with the same ring width placed in an increasing field. At 0 gauss, all the rings are in the vortex state. However, at 700G, two domain walls are nucleated in the smallest ring. This shows that the vortex state is not energetically favorable in rings of smaller outer diameter as compared to rings with a bigger outer diameter. We can understand this by examining the arrangement of moments in ring structures. Consider two rings of uniform ring width, a smaller ring versus a bigger ring. The magnetic moments around the width of the ring are more parallel in the ring with a greater outer diameter than the ring with the smaller outer diameter. We can see this illustrated in Figure 5.6 c) where the moments close to the inner edge of the ring bend more than they do at the outer edge of the ring. Therefore, there is a greater cost in exchange energy in smaller rings than in bigger rings. As a result, the vortex state has a much lower energy in the bigger ring making this state favorable.

Some of the challenges we have faced when imaging nanorings include weak probe magnetization and drift. Consistent MFM results depend on the tip maintaining uniform magnetization through out the scan. We hypothesize that the probes are showing weak magnetizations allowing the external field to
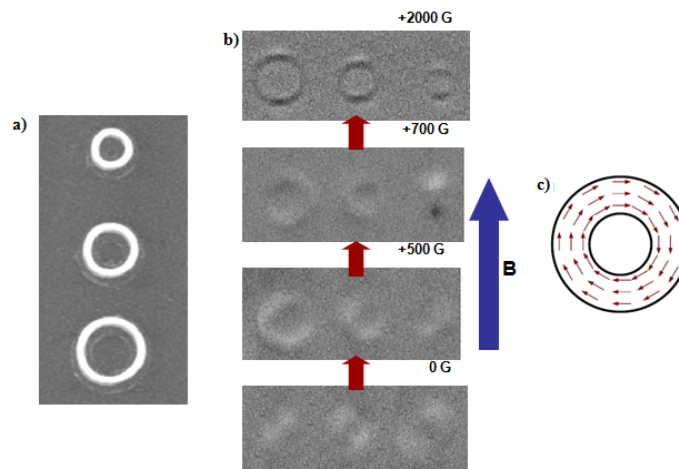
Figure 5.6: An illustration of how size affects the stability of magnetization (a) Topography image of the three rings of increasing outer diameter. (b) MFM image of the three rings at increasing fields. Notice that two domain walls are nucleated in the smallest ring first. (c) Alignment of magnetic moments showing how there is a bigger angle difference between sequential moments close to the inner circle versus the angle between sequential moments in close to the outer circle.

change the magnetization of the tip during imaging because we have observed the same dipole magnetization in rings exposed to a very negative field and in rings exposed to a very positive field. Using high coercivity tips eliminates this problem. The other issue we have faced includes drift. This is a more difficult problem to tackle because there are several causes for drift. Drift could be caused by loose AFM stage components, thermal fluctuations, a sample that is not well fixed on the stage and the rotation of the motor when one is using the variable field module. To eliminate drift, AFM stage components should be fixed in place and the sample should also be well mounted on the VFM stage. Drift as a result of thermal fluctuations often decreases after a few scans and

finally using a low motor speed when changing in-plane fields reduces drift due to the spinning of the motor.

5.3   Oersted Field

We would like to use the Oersted field from a current conducting AFM probe placed at the center of a ring to control the vortex chirality of the ring. We have begun to experimentally explore applying an azimuthal field. The first step in this process is to use the AFM to pass current through a conductive sample. We use a gold coated slide as our conductive sample. The AFM applies a voltage on the probe. Using contact imaging mode, we connect the sample and the tip. The rest of the circuit includes a resistor that is connected to the same ground reference as the AFM, forming a complete circuit pictured in Figure 5.7(a) We read the voltage across the resistor and plot a current-voltage curve. Figure 5.7(b) is an I-V curve obtained when we apply a bias ranging from -0.5V to 0.5V on a solid metal Rocky mountain probe in contact with a gold slide. This probe is made of platinum. The calculated resistance is $\approx$ 294 Ω which is much higher than our resistor value. The increased resistance could be due to the tip-gold connection that is difficult to achieve.

We have been able to answer a few questions at this preliminary stage. First, we have successfully tested our experimental set-up by obtaining reasonable I-V curves while using a conducting gold sample. Simulations predict that high current densities are necessary to induce switching in rings with a thickness of $\approx$ 5nm. This implies that we need to ensure that we can obtain high current values using our set-up. Currents as high as 10mA have been successfully passed using a platinum solid metal tip[26]. Our next step involves running current on a ring sample with a thin gold layer covering the silicon
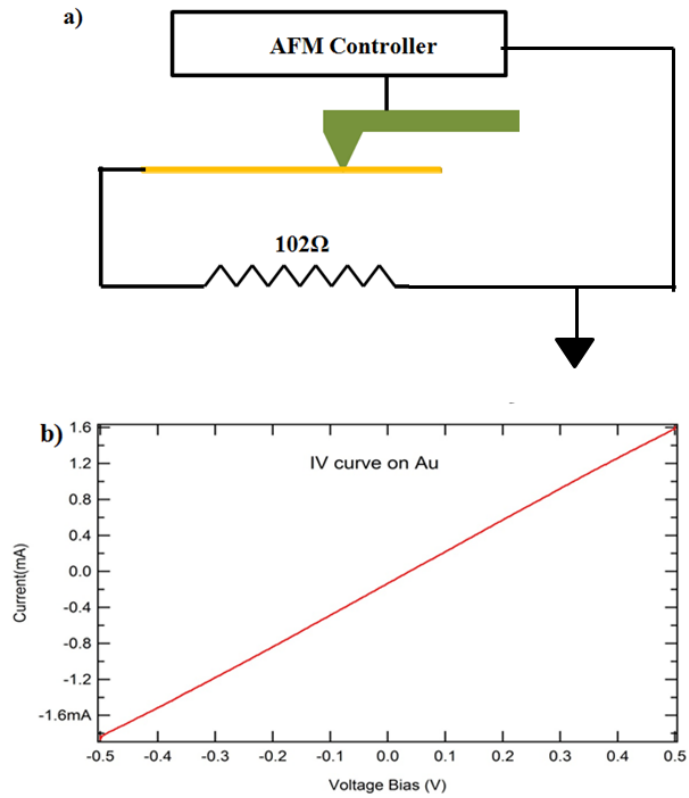
Figure 5.7: a) The experimental set up for running current through conductive sample using the AFM. b) I-V curve obtained when a bias in the range of -0.5 to 0.5 is applied on the sample

substrate.

Chapter 6

Conclusion

We would like to understand magnetization in nanoring structures in an external in-plane field and explore a new way to control vortex chirality in nanorings using an Oersted field. Nanorings are unique, in that they lack the energetically costly vortex core present in disks yet they display the low energy stray-field free vortex state even in nanorings with outer diameters as small as 10nm [13]. The clockwise and anti-clockwise vortex states in nanorings have been proposed as bit storage units. A comprehensive understanding of switching mechanisms into and out of the vortex state as well as the stability of the vortex state as a function of ring geometry is important for memory applications. Our research is focused on addressing these questions. In addition, we are investigating a new way to control chirality in nanoring structures using an Oersted field.

Our study of nanoring magnetization begins with fabricating nanoring arrays using electron beam lithography followed by a lift off process. We fabricate rings with different geometries. Samples that will be used to study magnetization reversal using an Oersted field are deposited on a gold coated

silicon wafer. We characterize the rings by atomic force microscopy obtaining the sample topography and imaging the magnetization of individual ring structures using magnetic force microscopy. We examine the evolution of magnetic states in nanoring structures using the variable field module which applies an in-plane field in the range of $\pm$ 2500 gauss.

We have measured a 1/2 ring hysteresis in nanoring structures. This study shows magnetization reversal processes that involve switching from the dipole state to the vortex state through the annihilation of two domain walls. We also observe switching from the vortex to the dipole state through the nucleation of two domain walls. Our studies on the size dependent stability of states reveal that the vortex state is more stable in rings with a bigger outer diameter than in rings with a smaller outer diameter.

We are interested in a new method of controlling vortex chirality in nanorings using an Oersted field. Our experimental implementation of this technique uses the AFM to apply a potential bias on the tip. The tip is placed in contact with a conductive sample. The sample is connected to a resistor and then to ground. This ground is shared by the resistor and the AFM creating a closed loop. Our goal is to use an Oersted field from a conducting probe placed at the center of nanoring to control vortex chirality. We have tested our experimental set-up obtaining promising results. Current-voltage curves when running current through a gold coated slide sample indicate that our set-up is working as it should. We have experimentally achieved currents as high as 10mA using a solid metal platinum tip and a gold coated slide sample. This demonstrates that we can attain high current densities required to cause reversal in rings with a thickness of a few nanometers.

Our next steps include verifying the results we have seen during MFM by repeating the experiment and completing the hysteresis loop. We would

like to image domain wall annihilation as it happens, observing the movement of one domain wall towards another. We will also further probe the geometry dependence of magnetization in ring structures obtaining the field range where certain states are stable given a particular ring geometry.

Our objectives also include using an Oersted field to change the vortex chirality of a ring structure, for example, an asymmetric ring and imaging the resulting vortex chirality through magnetic force microscopy. This is a challenging task that will involve marking rings to distinguish which rings were exposed to an Oersted field before performing magnetic force microscopy. Our research contributes to the fundamental understanding of magnetization in nanorings and possibly to memory applications.

Bibliography

[1] H. R. Varian, P. Lyman, *Journal of electronic publishing*, **6**, 2(2000)

[2] Hitachi, "Deskstar7K1000". Hitachi, 2007.

[3] C. L. Chien, F. Q. Zhu, J-G. Zhu *Physics today*, **40**,(2007)

[4] D. K. Singh, R. V. Krotkov, H. Q. Xiang, T. Xu, T. P. Rusell and M. T. Tuominen *Nanotechnology*, **19**, 245305(2008)

[5] OOMMF User's Guide, version 1.0, M. J Donahue and D. G. Porter, Interagency Report NISTIR 6376, NIST, Gaithersburg, MD (Sept 1999)

[6] The PC guide−IBM corporation, "http://www.pcguide.com", April 17th, 2001

[7] How stuff works, "http://computer.howstuffworks.com/hard-disk.htm".

[8] J-G Zhu, C. Park, *Materials Today*,**9, 11**,(2006)

[9] J-G Zhu, Y. Zheng, G. Prinz *Journal of Applied Physics*,**87, 9**,(2000)

[10] Giorgio Bertotti, *Hysteresis in magnetic materials for Physicists, material scientists and engineers*, (Academic, San Diego , 1998) p. 73

[11] Klaui M, Vaz CAF, Lopez-Diaz L, Bland J, *Journal of Physics: Condensed Matter*, **15**, R985 - R1023, (2003)

[12] What is a magnetic field?, "http://www.magnetic-shield.com/images/faq/flux-images.jpg", Magnetic Shield Corporation 1997 - 2008

[13] Zhang W, Haas S, *Handbook of Nanophysics*,(2010)

[14] Castano F, Ross C, Frandsen C, Eilez A, Gil D, Smith H, Redjdal M, Humphrey F, *Physical review B*, **67**, (2003)

[15] Klaui M, Vaz CAF, Bland J, Heyderman L, Nolting F, Pavlovska A, Bauer E, Cherifi S, Heun S, Locatelli A *Applied Physics Letters*,**18,23**,(2004)

[16] C A F Vaz et al., *Journal of Physics: Condensed matter*,**19**,(2007)

[17] P. Landeros, J. Escrig, D. Altbir *Journal of Applied Physics*,**100**,(2006)

[18] E. Saitoh, M. Kawabata, K. Harii and H. Miyajima*Journal of Applied Physics*,**95,4**,(2003)

[19] Stephen Blundell, *Magnetism in condensed matter*,Oxford University Press, New York, 2001 , P. 215

[20] W. Zhou, Z. L. Wang, Scanning Microscopy for Nanotechnology: Techniques and Applications. Springer, 2007.

[21] M. J. Marc, Fundamentals of Microfabrication: The Science of Miniaturization. 2nd edition, CRC Press LLC. New York, 2002.

[22] E. Meyer, H. Josef Hug, R. Bennewitz "Scanning Probe Microscopy: The lab on a tip". Springer, 2004.

[23] The Physics of Atomic Force Microscopy, www.AsylumResearch.com.

[24] Maya Farhoud, PhD Thesis, Characterization of Nanostructured Magnetic Particles for Application in Data Storage, 2000.

[25] Asylum Research, "http://www.asylumresearch.com/Products/Levers/AsyMFM.shtml".

[26] Katherine Aidala, Mark Tuominen et al. "Collaborative Proposal: Physics of Ferromagnetic Nanorings in an External Azimuthal Field" 2009.